Journal of Inorganic Biochemistry 241 (2023) 112134

Contents lists available at ScienceDirect

Journal of Inorganic Biochemistry

journal homepage: www.elsevier.com/locate/jinorgbio

Design, synthesis and biological evaluation of liposome entrapped iridium (III) complexes toward SGC-7901 cells

Yichuan Chen [a,1], Yiying Gu [a,1], Huiyan Hu [a], Haimei Liu [a], Wenlong Li [a], Chunxia Huang [a], Jing Chen [a], Lijuan Liang [a], Yunjun Liu [a,b,*]

[a] School of Pharmacy, Guangdong Pharmaceutical University, Guangzhou 510006, PR China
[b] Guangdong Provincial Key Laboratory of Advanced Drug Delivery, Guangdong Provincial Engineering Center of Topical Precise Drug Delivery System, Guangdong Pharmaceutical University, Guangzhou 510006, PR China

ARTICLE INFO

Keywords:
Iridium(III) complexes
Liposomes
Molecular docking
Immunogenic cell death
Endoplasmic reticulum

ABSTRACT

In this study, two new iridium(III) polypyridyl complexes [Ir(bzq)$_2$(DIPH)](PF$_6$) (bzq = deprotonated benzo[*h*]quinoline, DIPH = 4-(2,5-dibromo-4-(1*H*-imidazo[4,5-f][1,10]phenanthrolim-2-yl)-4-hydroxybutan-2-one) (**Ir1**) and [Ir(piq)$_2$(DIPH)](PF$_6$) (piq = deprotonated 1-phenylisoquinoline) (**Ir2**) were synthesized and characterized by elemental analysis, HRMS, ^{1}H and ^{13}C NMR. The cytotoxic activity of **Ir1**, **Ir2**, **Ir1lipo** and **Ir2lipo** against cancer cells SGC-7901, HepG2, A549, HeLa, B16 and normal NIH3T3 cells in vitro was evaluated using 3-(4,5-dimethylthiazole-2-yl)-2,5-biphenyl tetrazolium bromide (MTT) method. **Ir1** and **Ir2** showed no cytotoxic activity, but their liposome-entrapped **Ir1** (**Ir1lipo**) and **Ir2** (**Ir2lipo**) showed significant cellular activity, especially sensitive to SGC-7901 with IC$_{50}$ values of 4.7 ± 0.2 and 12.4 ± 0.5 μM, respectively. The cellular uptake, endoplasmic reticulum (ER) localization, autophagy, tubulin polymerization, glutathione (GSH), malondialdehyde (MDA) and release of cytochrome *c* were investigated to explore the mechanisms of apoptosis. The calreticulin (CRT), heat shock protein 70 (HSP70), high mobility group box 1 (HMGB1) were also explored. Western blotting showed that **Ir1lipo** and **Ir2lipo** inhibited PI3K (phosphoinositide-3 kinase), AKT (protein kinase B), p-AKT and activated Bcl-2 (B-cell lymphoma-2) protein and apoptosis-regulated factor caspase 3 (cysteinyl aspartate specific proteinase-3) and cleaving PARP (poly ADP-ribose polymerase). The results demonstrated that **Ir1lipo** and **Ir2lipo** induce cell apoptosis through targeting the endoplasmic reticulum (ER), cause oxidative stress damage, inhibiting PI3K/AKT signaling pathway, immunogenic cell death (ICD) and inhibit the cell growth at G2/M phase.

Abbreviations: A549, human lung carcinoma; AKT, protein kinase B; Annexin V-FITC, fluorescein isothiocyanate-labeled 3′,6′-dihydroxy-5-isothiocyanato-3H-spiro(isobenzofuran-1,9′-xanthen)-3-one; B16, Murine melanoma cells; Bad, Bcl-2 associated death promoter; Bax, Bcl-2 associated x protein; BCA, bicinchoninic acid; Bcl-2, B-cell lymphoma-2; bzq, benzo[*h*]quinoline; Calcein AM, Calcein Acetoxymethyl Ester; Caspase 3, cysteinyl aspartate specific proteinase-3; CHO-HP, cholesterol; CRT, calreticulin; DAMPs, damage associated molecular patterns; DAPI, 4′,6-diamidino-2-phenylindole; DIPH, 4-(2,5-dibromo-4-(1*H*-imidazo[4,5-f][1,10]phenanthrolim-2-yl)-4-hydroxybutan-2-one); DMEM, Dulbecco's Modified Eagle Medium; DMSO, dimethylsulfoxide; DSPE-mPEG2000, 1,2-distearoyl-sn-glycero-3-phosphoethanolamine-N-methoxy (polyethylene glycol)-2000; ER, endoplasmic reticulum; FAK, Focal adhesion kinase; FBS, Fetal bovine serum; FITC, fluorescein isothiocyanate; GSH, glutathione; HeLa, human cervical cancer cells; HepG2, human liver carcinoma cells; HMGB1, high mobility group box1; HSP70, heat shock protein 70; ICD, immunogenic cell death; MCTSs, multicellular tumor spheroids; MDA, malondialdehyde; MDC, monodansylcadaverine; MTT, 3-(4,5-dimethylthiazole-2-yl)-2,5-biphenyl tetrazolium bromide; NIH3T3, Mouse fibroblast cells; PARP, poly ADP-ribose polymerase; PBS, phosphate buffer solution; PC-98 T, Egg yolk lecithin; PCC, Pearson's correlation coefficients; PDI, Polydispersity index; PI, Propidium iodide; PI3K, phosphatidylinositol 3-kinase; piq, 1-phenylisoquinoline; PMSF, phenylmethylsulfonyl fluoride; PVDF, polyvinylidene difluoride; RIPA, 50 mM Tris (pH 7.4), 150 mM NaCl, 1% NP-40, 0.5% sodium deoxycholate; RLU, Relative luminometer units; RNase, ribonuclease; RPMI, 1640 Roswell Park Memorial Institute 1640; SDS-PAGE, sodium dodecyl sulfate polyacrylamide gel electrophoresis; SGC-7901, human gastric cells; TBA, thiobarbituric acid; TBST, 20 mM Tris–HCl, 150 mM NaCl, 0.2% Tween 20; TMS, tetramethylsilane; Tris, Tris(hydroxymethyl)aminomethane; Tween, 20 polysorbate 20.

* Corresponding author at: School of Pharmacy, Guangdong Pharmaceutical University, Guangzhou 510006, PR China.
E-mail address: lyjche@gdpu.edu.cn (Y. Liu).

[1] These authors ontribute equally to this work.

https://doi.org/10.1016/j.jinorgbio.2023.112134
Received 17 December 2022; Received in revised form 18 January 2023; Accepted 18 January 2023
Available online 21 January 2023

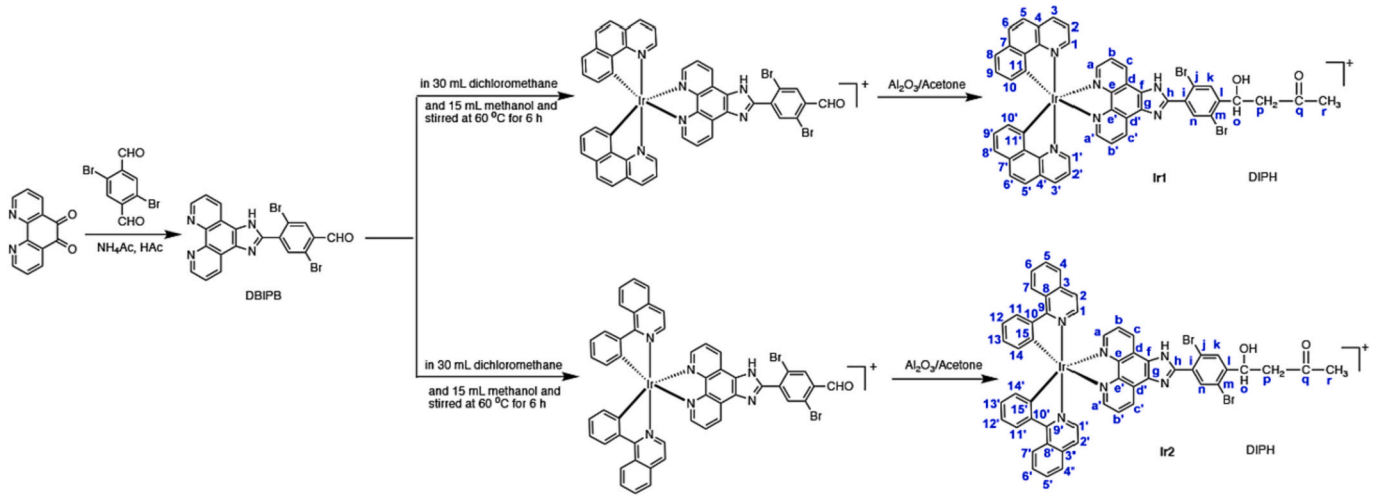

Scheme 1. Synthetic route of ligand and its complexes **Ir1** and **Ir2**.

1. Introduction

Cancer has become a major public health problem that poses a serious threat to human life and health [1,2]. Gastric cancer is one of the most common malignancies of the digestive system and is diagnosed in >1 million people worldwide each year [3,4]. Metastasis is the main cause of death in cancer patients [5]. However, malignant tumor cells often grow wildly and spread to other tissues or organs without control [6]. Tumor heterogeneity is a fundamental feature of malignancy, and gastric cancer poses a challenge for humans to overcome cancer due to its highly aggressive nature [7,8]. Chemotherapy remains an effective and commonly used method in the clinical treatment for recurrence and metastasis of cancer [9–12]. Since the discovery of cisplatin by Rosenberg et al. in the 1960s, the efficacy of platinum drugs such as carboplatin and oxaliplatin in cancer chemotherapy has been limited by side effects such as drug resistance, neurotoxicity, nephrotoxicity, hepatotoxicity, and bone marrow suppression [13–17]. In recent years, many metal complexes have been synthesized, among which iridium(III) complexes show great potential as promising anticancer candidates [18–30]. Compared to conventional dosage forms, nanodrugs have a higher delivery efficiency and are passively targeted to solid tumor tissue [31,32]. PEG-based liposomal drug delivery systems are widely recognized for producing extended circulation times and promoting tumor accumulation through enhanced permeability and retention effects [33–36]. In our previous studies [37–40], the low solubility of iridium(III) complexes makes them difficult to enter cells and exert anticancer activity. The liposomes loaded with iridium(III) complexes were able to greatly alter solubility and modify cellular dynamics and cellular uptake to enhance antitumor efficacy.

In order to obtain more information on the anticancer activity and further understanding the anticancer mechanism of iridium(III) complexes and their liposomes, in this work, two new iridium(III) complexes $[Ir(bzq)_2(DIPH)](PF_6)$ (bzq = deprotonated benzo[*h*]quinolone, DIPH = 2,5-dibromo-4-(1*H*-imidazo[4,5-*f*][1,10]phenanthrolin-2-yl)-4-hydroxybutan-2-one, **Ir1**) and $[Ir(piq)_2(DIPH)](PF_6)$ (piq = deprotonated 1-phenylisoquinoline, **Ir2**, Scheme 1) were synthesized characterized by elemental analysis, HRMS, ^1H and ^{13}C NMR. The **Ir1lipo** and **Ir2lipo** were characterized by size distribution, zeta potential, and release in vitro. The 3-(4,5-dimethylthiazole-2-yl)-2,5-biphenyl tetrazolium bromide (MTT) studies demonstrated that **Ir1** and **Ir2** showed no activity against the selected cancer cells SGC-7901, HepG2, A549, HeLa, B16 and normal NIH3T3 cells. To enhance the in vitro activity of **Ir1**, **Ir2**, the liposomes **Ir1lipo**, **Ir2lipo** were prepared by ethanol injection method. Surprisingly, **Ir1lipo** and **Ir2lipo** showed a strong inhibitory effect on the above tumor cells, especially on SGC-7901 cells.

In the present study, we determined the anticancer activity of **Ir1**, **Ir2**, **Ir1lipo** and **Ir2lipo** on SGC-7901 cells and investigated the cellular signal pathways associated with cell death. The results showed that complexes-loaded liposomes significantly increased cellular uptake and locate at the endoplasmic reticulum (ER), inhibited cellular glutathione (GSH) synthesis, increased malondialdehyde (MDA) levels leading to oxidative cellular damage and induced apoptosis. In addition, cytotoxicity of multicellular tumor spheroids (MCTSs), autophagy activation, microtubule protein inhibition, cytochrome *c*, Bcl-2 (B-cell lymphoma-2) family proteins and immunogenic cell death (ICD) were also investigated. **Ir1lipo** and **Ir2lipo** induced apoptosis mainly through inhibiting the PI3K/AKT signaling pathway and further activated the Bcl-2 (B-cell lymphoma-2) protein and caspase 3, upregulated the cleaved PARP (poly ADP-ribose polymerase). Furthermore, the results from the calreticulin (CRT) exposure, heat shock protein 70 kDa (HSP70) and high mobility group box 1 (HMGB1) further confirm that **Ir1lipo** and **Ir2lipo** can lead to immune cell death (ICD).

2. Experimental

2.1. Materials and methods

All chemicals and reagents used in the experiments commercially were purchased and used directly without further purification unless otherwise stated. $IrCl_3{\cdot}3H_2O$ was obtained from the Kunming Boren Precious Metals Co., Ltd. MTT (3-(4,5-dimethylthiazol-2-yl)-2,5-diphenyl-2H-tetrazolium bromide) was purchased from Sigma–Aldrich (St. Louis, MO, USA; 98% purity). Human gastric cells SGC-7901, Human liver carcinoma cells HepG2, Human lung carcinoma A549, Human cervical cells HeLa, Murine melanoma cells B16, Mouse fibroblast cells NIH3T3 were gained from the Cell Center of Sun Yat-Sen University (Guangzhou, China). High glucose Dulbecco's modified Eagle's medium (DMEM), Roswell Park Memorial Institute (RPMI) 1640 were purchased from Corning Corp (New York, USA) and Fetal bovine serum (FBS) was obtained from Gibco Corporation. PC-98 T (Egg yolk lecithin), CHO-HP (cholesterol) and 1,2-distearoyl-sn-glycero-3-phosphoethanolamine-N-methoxy (polyethylene glycol)-2000 (DSPE-mPEG2000) were purchased from AVT Pharmaceutical Tech Co., Ltd. (Shanghai, China). Propidium iodide (PI), Annexin V-FITC Apoptosis Detection Kit, Hoechst and ER-Tracker Red were obtained from Beyotime Institute of Biotechnology (Shanghai, China). CRT, HMGB1 and HSP70 Rabbit Polyclonal Antibody, FITC-labeled Goat Anti-Rabbit IgG were purchased from Beyotime Institute of Biotechnology (Shanghai, China). Microanalysis (C, H, and N) was carried out with a Perkin–Elmer 240Q elemental analyzer. ^1H and ^{13}C NMR spectra were recorded on a

Varian-500 spectrometer with DMSO-d_6 as a solvent and tetramethylsilane (TMS) as an internal standard at room temperature. The spray voltage, tube lens offset, capillary voltage and capillary temperature were set at 4.50 kV, 30.00 V, 23.00 V and 200 °C, respectively, and the quoted *m/z* values are for the major peaks in the isotope distribution.

2.2. Synthesis of complexes

2.2.1. Synthesis of the ligand DBIPB

A mixture of 1,10-phenanthroline-5,6-dione (0.315 g, 1.5 mmol) [41], 2,5-dibromo-1,4-benzenedicarbroxadehyde (0.437 g, 1.5 mol), NH_4Ac (3.08 g, 40 mmol) was dissolved in glacial acetic acid (25 mL) and refluxed at 130 °C for 2 h, then cool to room temperature. A saturated aqueous ammonium solution (25 mL) was added to neutralize the solution to obtain a yellow precipitate, which was filtered and washed with ice water. After dissolution in anhydrous ethanol, the yellow solid was collected after recrystallization and dried under a vacuum. Yield: 85%. ESI-MS (CH_3OH): *m/z* = 480.87 ([M − 1]). Anal. Calcd for $C_{20}H_{10}Br_2N_4O$: C, 49.82, H, 2.09, N, 11.62%. Found: C, 49.70, H, 2.25, N, 11.81%. IR (KBr, cm^{-1}): 3355 m, 3064 w, 1783 w, 1687 s, 1618 s, 1571 s, 1434 w, 1352 w, 1261 w, 1178 s, 1128 w, 1054 s, 804 s, 734 s.

2.2.2. Synthesis of $[Ir(bzq)_2(DIPH)]PF_6$ (**Ir1**)

A mixture of cis-$[Ir(bzq)_2Cl]_2$ (0.30 g, 0.25 mmol) [42] and DBIPB (0.24 g, 0.5 mmol) in a mixture of 30 mL of dichloromethane and methanol (*v*/v, 2:1) was heated and refluxed at 40 °C for 6 h under argon to obtain a yellow solution. After cooling, excessive NH_4PF_6 powder was added to the solution, stirred for 2 h and the filtrate was collected and dried under vacuum to obtain a yellow intermediate product $[Ir(bzq)_2(DBIPB)](PF_6)$. Next, the intermediate product was purified by column chromatography on Al_2O_3 (pH = 7.05, weak alkaline) with a mixture of dichloromethane and acetone (*v*/v, 1:3) as eluent. During the purification process, the aldehyde group in DBIPB with acetone underwent an aldehyde and ketone condensation reaction to produce the complex $[Ir(bzq)_2(DIPH)](PF_6)$. Finally, the yellow band was collected. The solvent was removed by evaporation under reduced pressure and the yellow powder was obtained after vacuum drying. Yield: 77%. Anal Calcd for $C_{49}H_{32}Br_2IrN_6O_2PF_6$: C, 47.70, H, 2.61, N, 6.81%. Found: C, 47.51, H, 2.84, N, 6.97%. HRMS (CH_3CN): Calcd for $C_{49}H_{32}Br_2IrN_6O_2PF_6$ *m/z* = 1089.0560 ($[M\text{-}PF_6]^+$), found: *m/z* = 1089.1400 ($[M\text{-}PF_6]^+$) (Fig. S1a, supporting information). IR (KBr cm^{-1}, Fig. S1b, supporting information): 3439 s, 3043 m, 2923 m, 1706 m, 1620 m, 1567 m, 1446 s, 1354 m, 1329 m, 1191 m, 1081 m, 1051 m, 846 s, 722 m, 558 m. ^1H NMR (DMSO-d_6, 500 MHz, Fig. S1c, supporting information): The H proton in the imidazole ring was not observed, 9.10 (d, 1H, H_a, *J* = 8.0 Hz), 9.05 (d, 1H, $H_{a'}$, *J* = 7.0 Hz), 8.52–8.50 (m, 2H, $H_{1,1'}$), 8.13 (s, 1H, H_k), 8.03 (d, 2H, $H_{c,c'}$, *J* = 4.5 Hz), 7.99–7.96 (m, 4H, $H_{3,3',8,8'}$), 7.92 (s, 1H, H_n), 7.88 (d, 2H, $H_{5,5'}$, *J* = 3.0 Hz), 7.85 (d, 2H, $H_{6,6'}$, *J* = 3.5 Hz), 7.58 (d, 1H, H_{10}, *J* = 3.0 Hz), 7.56 (d, 1H, $H_{10'}$, *J* = 4.0 Hz), 7.47–7.42 (m, 2H, $H_{9,9'}$), 7.24–7.20 (m, 2H, $H_{b,b'}$), 6.34 (t, 2H, $H_{2,2'}$, *J* = 6.0 Hz), 5.30 (t, 1H, H_o, *J* = 4.0 Hz), 4.57 (s, 1H, H_{OH}), 2.72 (d, 2H, H_p, *J* = 8.5 Hz), 2.20 (s, 3H, $H_{\text{-}CH3}$). ^{13}C NMR (DMSO-d_6, 125 MHz, Fig. S1d, supporting information): 207.99 (C_q), 158.51 (C_h), 150.68 ($C_{a,a'}$), 149.80 (C_1), 149.72 ($C_{1'}$), 145.92 ($C_{13,13'}$), 142.43 (C_l), 139.45 (C_i), 137.08 ($C_{e,e'}$), 135.75 ($C_{3,3'}$), 134.45 (C_n), 133.89 ($C_{7,7'}$), 131.72 (C_k), 131.50 ($C_{c,c'}$), 130.59 ($C_{12,12'}$), 128.69 ($C_{5,5',6,6',8,8'}$), 128.36 ($C_{11,11'}$), 128.28 ($C_{4,4'}$), 126.21 ($C_{d,d'}$), 124.75 ($C_{9,9',10,10'}$), 122.75 ($C_{f,g}$), 122.25 (C_m), 121.62 ($C_{2,2',b,b'}$), 121.30 (C_j), 70.55 (C_o), 57.83 (C_p), 31.60 (C_r).

2.2.3. Synthesis of $[Ir(piq)_2(DIPH)]PF_6$ (**Ir2**)

Complex $[Ir(piq)_2(DBIPB)](PF_6)$ was synthesized and purified as the same method described for $[Ir(bzq)_2(DBIPB)](PF_6)$, with cis-$[Ir(piq)_2Cl]_2$ (0.38 g, 0.25 mmol) [42] in place of cis-$[Ir(bzq)_2Cl]_2$ (0.30 g, 0.25 mmol). During the process of purification, $[Ir(piq)_2(DBIPB)](PF_6)$ was transferred into $[Ir(piq)_2(DIPH)](PF_6)$. Yield: 79%. Anal Calcd for $C_{53}H_{36}Br_2IrN_6O_2PF_6$: C, 49.50, H, 2.82, N, 6.54%. Found: C, 49.84, H, 2.61, N, 6.84%. HRMS (CH_3CN): Calcd for $C_{53}H_{36}Br_2IrN_6O_2PF_6$ *m/z* = 1141.0875 ($[M\text{-}PF_6]^+$), found: *m/z* = 1141.0829 ($[M\text{-}PF_6]^+$) (Fig. S2a, supporting information). IR (KBr, cm^{-1}, Fig. S2b, supporting information): 3425 m, 3042 m, 2922 m, 1075 m, 1606 m, 1575 m, 1539 m, 1444 s, 1379 m, 1351 s, 1270 m, 1148 m, 1079 m, 1048 s, 843 m, 729 m, 557 m. ^1H NMR (DMSO-d_6, 500 MHz, Fig. S2c, supporting information): The H proton in the imidazole ring was not observed, 9.11 (dd, 2H, $H_{a,a'}$, *J* = 3.0 Hz, *J* = 7.0 Hz), 9.06–9.02 (m, 2H, $H_{1,1'}$), 8.44 (s, 1H, H_k), 8.41–8.39 (m, 2H, $H_{c,c'}$), 8.16 (s, 1H, H_n), 7.99 (t, 2H, $H_{11,11'}$, *J* = 7.0 Hz), 7.90–7-83 (m, 8H, $H_{7,7',b,b',4,4',2,2'}$), 7.45 (t, 2H, $H_{5,5'}$, *J* = 6.5 Hz), 7.40–7.37 (m, 2H, $H_{6,6'}$), 7.18–7.15 (m, 2H, $H_{14,14'}$), 6.97–6.93 (m, 2H, $H_{12,12'}$), 6.33 (t, 2H, $H_{13,13'}$, *J* = 7. 0 Hz), 5.28 (t, 1H, H_o, *J* = 5.5 Hz), 4.58 (s, 1H, H_{OH}), 2.70 (d, 2H, H_p, *J* = 8.5 Hz), 2.19 (s, 3H, $H_{\text{-}CH3}$). ^{13}C NMR (DMSO-d_6, 125 MHz, Fig. S2d, supporting information): 207.98 (C_q), 158.55 ($C_{9,9'}$), 158.52 (C_h), 150.68 ($C_{a,a'}$), 150.65 ($C_{1,1'}$), 149.82 (C_l), 149.73 (C_i), 145.91 ($C_{e,e',10,10'}$), 142.43 ($C_{3,3'}$), 139.45 ($C_{n,k}$), 138.39 ($C_{c,c'}$), 137.08 ($C_{5,5'}$), 135.75 ($C_{12,12'}$), 134.45 ($C_{14,14'}$), 133.89 ($C_{8,8'}$), 131.72 ($C_{11,11'}$), 131.51 ($C_{13,13',6,6'}$), 130.59 ($C_{15,15'}$), 128.69 ($C_{4,4'}$), 128.34 ($C_{d,d'}$), 128.26 ($C_{7,7'}$), 126.21 ($C_{f,g}$), 124.75 ($C_{b,b'}$), 122.25 (C_m), 121.69 (C_j), 121.30 ($C_{2,2'}$), 70.54 (C_o), 57.82 (C_p), 31.60 (C_r).

2.3. Preparation of the liposomes

Liposomes **Ir1lipo** and **Ir2lipo** were prepared using the ethanol injection method [43]. Briefly, 1 mg of **Ir1** or **Ir2**, 500 μL of PC-98 T (60 mg/ml), 8 mg of CHO-HP and 5 mg of DSPE-mPEG2000 were thoroughly mixed and completely dissolved in anhydrous ethanol. Next, the mixture was slowly injected into the 5 mL PBS (phosphate buffer solution) at 55 °C with stirring for 20 min to discard absolute ethanol. After that, the PBS was slowly added to the mixture solution to form a 5 mL solution and sonicated using an ultrasonic cell disrupter with the presetting parameters (150 W, 5 min, 1 s on/off) in an ice bath. At the end of sonication, the solution was centrifuged (10,000 rpm, 4 °C) for 10 min and the supernatant was collected and stored at 4 °C.

2.4. Particle size and surface potential of the liposomes

The mean particle diameter and zeta potential of **Ir1lipo** and **Ir2lipo** were measured using Zetasizer Nano ZS-90 (Malvern, UK). Each sample was diluted with ultrapure water (1: 5) tested at 25 °C and repeated three times.

2.5. Determination of encapsulation efficiency (EE%)

The **Ir1** or **Ir2** content in liposomes was quantified via the UV–Vis spectrometer. In brief, the complexes were dissolved in absolute ethanol to prepare different concentrations (5, 7.5, 10, 12.5, 15 and 20 μg/mL) of solutions, and the relationship between concentration and absorbance values (standard curve) was obtained by UV–Vis spectroscopy of the above six solutions. Next, 1 mL liposome was dissolved in 10 mL absolute ethanol under sonication for 3 h to completely extract the incorporated **Ir1** or **Ir2**. Then the solutions were filtered through a membrane (0.22 μM diameter) and **Ir1** or **Ir2** concentration was measured using a Perkin Elmer Lambda UV–Vis spectrometer (Perkin-Elmer, UK). The encapsulation efficiency (EE) was calculated using the following equation:

$$EE(\%) = \frac{E_{drug}}{T_{drug}} \times 100\%$$

where E_{drug} represents the amount of complex encapsulated in the liposome and T_{drug} represents the amount of total complex initially added.

2.6. Drug release in vitro from liposome

In vitro the release of **Ir1lipo** and **Ir2lipo** in phosphate buffered saline (PBS, pH = 7.4) containing 0.5% Tween 80 (*w/v*) was determined by the dialysis method. 4 mL of **Ir1lipo** and **Ir2lipo** were filtered through a membrane (0.22 μM diameter) and placed in a dialysis bag (8–14 kDa molecular weight) in 200 mL PBS solution which was continuously stirred at 37 °C (100 rpm). Samples (3 mL) were collected at the different time intervals (0.5, 1, 2, 4, 6, 8, 10, 12, 16, 20, 24, 30, 36, 48, 60, 72 and 84 h) and supplied with an equal amount of fresh PBS (0.5% Tween 80). The concentrations of **Ir1** and **Ir2** were measured by UV–Vis spectroscopy.

2.7. pK_a of the complex determination

The pK_a values of the complexes were determined by potentiometric titration method using a pH meter (Basic pH Meter PB-10, Sartorius). Firstly, 100 μM of **Ir1** or **Ir2** was dissolved in a mixture of acetonitrile and water (*v*/v, 3:7), HCl (100 mM) and KOH (60 mM) were prepared. The pH values were slowly decreased to about pH 2.0 through gradually titrating with 100 mM of HCl, then NaOH solution was gradually added, the change in pH was recorded by slowly dropping a KOH solution (60 mM) into the above solution.

2.8. Cell culture

SGC-7901 cells were cultured with RMPI-1640 medium and HepG2, A549, HeLa, B16, NIH3T3 cells were cultured with DMEM medium supplemented with 10% (*v*/v) fetal bovine serum (FBS) (Gibco), 100 U/mL penicillin and 0.1 mg/mL streptomycin in a humidified incubator containing 95% air and 5% CO_2 at 37 °C.

2.9. Cell viability assay of 3D culture

SGC-7901 cells in the exponential growth phase were dissociated by trypsinization and centrifuged for 5 min at 1000 *g* to gain single-cell suspensions. Diluted SGC-7901 cells suspensions (5.0×10^4, 200 μL) were transferred to 100 μL Matrigel matrix (Corning) confocal petri dish with RPMI 1640 (200 μL) containing 10% FBS at 37 °C for 30 min. Next, 200 μL of Matrigel and RPMI 1640 (*v*/v, 1:9) was slowly added into the confocal Petri dishes to produce a gel-cell-gel structure. The single cells were cultured at 37 °C with 5% CO_2 and SGC-7901 multicellular tumor spheroids (MCTSs) appeared on day 4. After treatment with treated with IC_{50} of **Ir1**, **Ir2**, **Ir1lipo** and **Ir2lipo** for 24 h, the cells were stained with Calcein-AM (Calcein Acetoxymethyl Ester)/PI (Meilum Biotechnology, Dalian) and Hoechst for 30 min and imaged under a confocal microscope (Leica TCS-SP8 SR, Germany).

2.10. Cytotoxicity assay in vitro

The cytotoxic activity in vitro of **Ir1**, **Ir2**, **Ir1lipo** and **Ir2lipo** against the selected cancer cells lines SGC-7901, A549, HepG2, HeLa, B16 and normal NIH3T3 cells was evaluated using 3-(4,5-dimethylthiazole-2-yl)-2,5-biphenyl tetrazolium bromide (MTT) method [44]. The cells (1×10^4 cells per well, 100 μL) were placed in 96-well culture plates (Corning) and grew overnight at 37 °C in a 5% CO_2 incubator. When the cells reached 70% growth, the complexes and liposomes were added to the wells at different concentrations (0–100 μM) and blank liposomes were added as the control group. After 48 h, the medium in the wells was removed and replaced with 9 mL of medium and 1 mL of MTT dye solution (100 μL, 5 mg/mL) and incubation was continued for 4 h at 37 °C. Next, the suspension was replaced with DMSO (100 μL/well) to solubilize the MTT formazan. The absorbance of each well was measured under a microplate spectrophotometer (Multiskan FC, Thermo Scientific, Shanghai, China) at a wavelength of 490 nm. The IC_{50} values were obtained from the analysis of absorbance data from three independent experiments using IBM SPSS Statistics (version 20.0).

2.11. Cellular uptake

The well-growing SGC-7901 cells were cultured in 12-well plates (1×10^5 cells per well) in an incubator overnight and exposed to IC_{50} concentrations of **Ir1**, **Ir2**, **Ir1lipo** and **Ir2lipo** for 24 h. The cell nuclei were stained with (4′,6-diamidino-2-phenylindole) DAPI (5 μg/mL in PBS) for 20 min at 37 °C followed by washing twice with cold PBS. The cell images were captured under the ImageXpress R Micro XLS System (MD company, USA) and the uptake extent in SGC-7901 cells of the complexes and liposomes were analyzed using a flow cytometer (Beckman Instruments, NJ).

2.12. Wound healing in vitro

The in vitro wound healing assay is an effective and convenient method for detecting the collective migration of SGC-7901 cells. The cells (5.0×10^5 cells per well) were seeded in 6-well plates and cultured overnight. After creating a scratch with a sterile pipette tip, the monolayer was washed with PBS to remove any residual cell debris and a fresh medium containing 1% FBS was added. The cells were treated with IC_{50} concentration of **Ir1**, **Ir2**, **Ir1lipo** and **Ir2lipo** for 24 h in an incubator at 37 °C, 5% CO_2 and 95% air. Finally, the cells were photographed at 0 and 24 h under an inverted microscope (Olympus Co., Tokyo, Japan).

2.13. Localization of the complexes in the endoplasmic reticulum

SGC-7901 cells (1×10^5 cells/well) were seeded in 12-well plates (1 mL/well) in RPMI 1640 medium overnight. Thereafter, the IC_{50} concentration of the complexes and liposomes were added and incubated for 4 h. After that, the cells were washed two times with cold PBS and stained with 500 μL of a solution of ER Tracker Red (1 μM, Beyotime Biotechnology, Shanghai, China) at 37 °C for 20 min in the dark. The nuclei were stained with Hoechst (10 μg/mL) for 20 min. Subsequently, the cells were washed twice, and the images were acquired under an ImageXpress Micro XLS System as soon as possible.

2.14. Measurement of glutathione (GSH) and malondialdehyde (MDA) content

GSH and GSSG contents were measured by GSH and GSSH Assay Kit (S0053, Beyotime Biotechnology, Shanghai, China). SGC-7901 cells (5×10^5 cells per well) were seeded in 6-well plates and inoculated overnight. Next, after treatment with IC_{50} concentrations of **Ir1**, **Ir2**, **Ir1lipo** and **Ir2lipo** for 24 h, SGC-7901 cells were collected, centrifugated and the supernatant was collected. According to the manufacturer's instructions, total glutathione was measured at 412 nm using a microplate reader (BioTek, Winooski, USA), and GSH content was obtained by subtracting the amount of GSSG from the total glutathione. The MDA levels were quantified using the Lipid Peroxidation MDA Assay Kit (S0131S, Beyotime Biotechnology, Shanghai, China). In brief, the SGC-7901 of supernatant was prepared in lysis buffer and centrifuged (12,000 *g*, 15 min, 4 °C). The samples were treated with TBA (thiobarbituric acid) in the boiling water bath for 40 min and the absorbance was measured at 530 nm. MDA levels were expressed as μmol/g protein.

2.15. Measurement of apoptosis

Annexin V-FITC/PI double staining method was used to assess the apoptosis of the SGC-7901 cells. Logarithmic growth phase SGC-7901 cells (5×10^5 cells per well) were seeded into 6-well plates and cultured overnight. When the cells reached 70%, the cells were treated with IC_{50} concentrations of **Ir1**, **Ir2**, **Ir1lipo** and **Ir2lipo** at 37 °C in 5% CO_2 for 24 h. Next, after removing the medium, the cells were washed twice with cold PBS and centrifuged at 1000 rpm for 5 min. Finally, the

cells were resuspended Annexin V binding buffer (195 μL) and stained with 1 mg/mL of Annexin V-FITC (5 μL) and 500 mg/mL of pyridine iodide (10 μL) at 37 °C in the dark for 20 min. The apoptosis was immediately determined by flow cytometry (Beckman Instruments, NJ) and the obtained results were analyzed with Flow Jo (version 10.0).

2.16. Analysis of cell cycle arrest

To further investigate the effect of complexes and liposomes on the inhibition of SGC-7901 cells proliferation, the cell cycle distribution was measured by flow cytometry analysis. The cells were seeded in 6-well plates at a density of 5×10^5 cells/well and incubated in RPMI 1640 supplemented with 10% FBS for 24 h. After treatment with IC_{50} concentrations of complexes and liposomes for 24 h, the cells were collected and fixed in 75% ethanol at 4 °C overnight. Next day, the cell pellets were washed twice with cold PBS and resuspended in 200 μL of assay buffer with 0.1% Triton X-100, 4 μL of PI (propidium iodide, 0.02 mg/mL) and 4 μL of RNase A (ribonuclease, 0.2 mg/mL) for 30 min at 37 °C in the dark. Analysis of samples was performed using a flow cytometer (Beckman Instruments, NJ).

2.17. Release of cytochrome c

SGC-7901 cells were seeded in a 12-well plate (1×10^5 cells/well) and cultured overnight at 37 °C in a 5% CO_2 incubator. Then the cells were treated with IC_{50} concentration of the complexes and liposomes for 24 h. The cells were fixed with cold immunol staining fixed solution for 30 min and blocked with immunol staining blocking buffer for 1 h at room temperature. Next, the cells were treated with the primary antibody against cytochrome *c* (1:50 dilution) overnight at 4 °C. Subsequently, after washing three times with immunol staining wash buffer, SGC-7901 cells were incubated overnight by Anti-Mouse FITC conjugated IgG antibody (1:500 dilution) in the dark for 1 h at room temperature. Finally, the images were acquired under the ImageXpress Micro XLS system (MD company, USA).

2.18. Measurement of CRT, HSP70, HMGB1

SGC-7901 cells (1×10^5 cells/well) were seeded in the 12-well plate overnight, then the cells were treated with IC_{50} concentration of **Ir1**, **Ir2**, **Ir1lipo** and **Ir2lipo**. After 24 h, the cells were washed with cold PBS three times, fixed with alcohol (75%) and blocked with immunol staining blocking buffer for 1 h at room temperature. Next, after washing three times with immunol staining wash buffer, the cells were incubated with primary antibodies (CRT, HSP70 and HMGB1) at 1:70 dilutions at 4 °C overnight. After that, FITC-labeled Goat Anti-Rabbit IgG was added and incubated in dark for 1 h and Hoechst was used to stain the nuclei. Finally, the cells were washed twice with PBS, then photographed immediately under the ImageXpress Micro XLS System.

2.19. Cellular autophagy studies

SGC-7901 cells were placed into a 12-well plate and incubated overnight. Then, the medium was discarded and replaced with fresh medium containing IC_{50} concentration of **Ir1**, **Ir2**, **Ir1lipo** and **Ir2lipo** in an incubator at 37 °C, 5% CO_2 and 95% air for 24 h. After that, the cells were washed three times with cold PBS and stained with 50 μM of MDC (monodansylcadaverine) at 37 °C for 30 min in the dark. Finally, the cells were imaged under the ImageXpress Micro XLS system.

2.20. Effect on microtubules networks

SGC-7901 cells were grown in 12-well culture plates at a density of 1×10^5 cells per well and exposed to the complexes and liposomes with IC_{50} concentration for 24 h. Next, the cells were washed three times with cold PBS and fixed overnight at 4 °C with cold immunol staining fix solution and incubated with immunol staining blocking buffer for 70 min. After washing 3 times with immunol staining wash buffer, the cells were incubated with anti-rabbit monoclonal anti-α-tubulin antibody (1:100 dilution) overnight at 4 °C followed by anti-rabbit FITC conjugated IgG antibody (1:500 dilution) for 1 h. Subsequently, the cells were washed with immunol staining wash buffer three times and the cell nuclei were stained with DAPI (10 mg/mL) for 30 min. Eventually, the cells were visualized and imaged by the ImageXpress Micro XLS System.

2.21. Western blot analysis

SGC-7901 cells were seeded into 6-well plates at a density of 5.0×10^5 cells per well and incubated overnight. After treatment with **Ir1**, **Ir2**, **Ir1lipo** and **Ir2lipo** for 24 h, SGC-7901 cells were lysed in RIPA (50 mM Tris pH = 7.4, 150 mM NaCl, 1% NP-40, 0.5% sodium deoxycholate) buffer containing 1 mM PMSF (phenylmethylsulfonyl fluoride) by centrifugation (12,000 *g*, 4 °C, 15 min) to extract proteins. The protein concentrations were determined by BCA (bicinchoninic acid) Protein Assay Kit (P0012S, Beyotime Biotechnology, Shanghai, China). The protein samples (20 μL) with equal concentration were separated through 10 or 15% sodium dodecyl sulfate polyacrylamide gel electrophoresis (SDS-PAGE) and transferred onto polyvinylidene difluoride (PVDF) membranes (Millipore Sigma, USA). After three washes with TBST (20 mM Tris–HCl, 150 mM NaCl, 0.2% Tween 20, pH = 8.0), the PVDF membranes were incubated with primary antibodies (1:5000 dilution) overnight at 4 °C, followed by the corresponding secondary antibodies for 70 min. Finally, after being washed with TBST four times, the PVDF membranes were visualized using BeyoECL Star and the blots were imaged using a FluorChemE (ProteinSimple, CA, USA). The protein expression levels were quantified with Image J software and normalized to the control β-actin.

2.22. Molecular docking studies

The molecular structure of all candidate drug compounds obtained from PubChem databank (https://pubchem.ncbi.nlm.nih.gov/) and drawn by ChemBioDraw Ultra 17.0. The crystal structures of p53 (PDB ID: 4BUZ), CDK1 (PDB ID: 5LQF), p21(PDB ID: 5E0U), PARP (PDB ID: 4PJV), PI3K (PDB ID: 1E8X), Caspase 3 (PDB ID: 1GFW), Bad (PDB ID: 1G5J), Bax (PDB ID: 2K7W) and Bcl-2 (PDB ID: 4LVT) were downloaded from the RCSB protein data bank (PDB) (http://www.rcsb.org/). Autodock Vina 1.2.2 was used to detect the binding energy and interaction patterns between drugs and targets.

2.23. Data analysis

All data were expressed as mean ± SD. Statistical significance was evaluated using *t*-tests. The difference was significant when the $^*P$ value was <0.05.

3. Results and discussion

3.1. Synthesis and characterization

The ligand DBIPB was obtained by the direct reaction of 1,10-phenanthroline-5,6-dione with 2,5-dibromoterephthalaldehyde in the glacial acetic acid. The intermediates $[Ir(bzq)_2(DBIPB)](PF_6)$ and $[Ir(piq)_2(DBIPB)](PF_6)$ were synthesized with $[Ir(bzq)_2Cl_2]_2$ or $[Ir(piq)_2Cl_2]_2$ and DBIPB in a mixture of dichloromethane and methanol (*v*/v, 2:1) as a solvent under argon. Finally, the intermediate product was purified by column chromatography on Al_2O_3 (pH = 7.05, weak alkaline) with a mixture of dichloromethane and acetone (v/v, 1:3) as eluent. Unexpectedly, in the process of purification, owing to an occurrence of aldehyde and ketone condensation reaction, complexes $[Ir(bzq)_2(DBIPB)](PF_6)$ and $[Ir(piq)_2(DBIPB)](PF_6)$ were transferred into $[Ir(bzq)_2(DIBH)](PF_6)$ (**Ir1**) and $[Ir(piq)_2(DIBH)](PF_6)$ (**Ir2**).

The synthesized complexes **Ir1** and **Ir2** were characterized by HRMS, UV–Vis, ^{1}HNMR and ^{13}CNMR. In the IR spectra, the peaks at 3355 cm^{-1} for DBIPB, 3439 cm^{-1} for **Ir1** and 3425 cm^{-1} for **Ir2** are attributed to the N—H (imidazole ring) stretching vibration. The peaks of 3064, 3043, 3042 cm^{-1} for DBIPB, **Ir1** and **Ir2** are assigned to C—H stretching vibration. The peaks of 1783, 1706 and 1705 cm^{-1} are assigned to the aldehyde group of DBIPB and carboxyl groups of **Ir1** and **Ir2**, respectively, the peaks of 846 cm^{-1} for **Ir1** and 843 cm^{-1} for **Ir2** are assigned to the stretching vibration of P—F bond, and the peaks of 558 cm^{-1} for **Ir1** and 557 cm^{-1} for **Ir2** are attributed to the bending vibration of P—F bond (PF_6^-). In the HRMS spectra, the determined molecular weights are consistent with the expected values.

In the ^{1}H NMR spectra, for the **Ir1**, the peaks of 8.13 (s, 1H) and 7.92 (s, 1H) are assigned to the hydrogens of H_k and H_n, the peaks of 5.30 (t, 1H), 4.57 (s, 1H), 2.72 (d, 2H) and 2.20 (s, 3H) are attributed to the hydrogens of H_o, H_{OH}, H_p and H_r (-CH_3). For the **Ir2**, the peaks of 8.44 (s, 1H) and 8.17 (s, 1H) are assigned to the hydrogens of H_k and H_n, the peaks of 5.28 (t, 1H), 4.58 (s, 1H), 2.70 (d, 2H) and 2.19 (s, 3H) are attributed to the hydrogens of H_o, H_{OH}, H_p and H_r (-CH_3). While the peak for the proton on nitrogen atom of the imidazole ring was not observed. This may be caused by metal coordination inducing electron deficiency in the ligand, therefore, the NH proton of the imidazole ring is very active and easy to be exchanged between the two imidazole nitrogen atoms in solution.

In the ^{13}C NMR spectra, the peaks of 207.99, 70.55, 57.83 and 31.60 ppm for **Ir1** are attributed to the carboxyl group C_q, C_o, C_p and C_r, respectively. The peaks of 207.98, 70.54, 57.82 and 31.60 ppm for **Ir2** are assigned to the carboxyl group C_q, C_o, C_p and C_r, respectively.

The stability of the complexes in PBS solution was determined, as shown in Fig. S3 (supporting information), the peak shapes of the complexes have no change at 0 and 48 h, indicating that the complexes are stable in PBS solution.

The ethanol injection method was used with the mole ratio of 5:8:30 of DSPE-mPEG2000, CHO-HP and PC-98 T to produce stable **Ir1lipo** and **Ir2lipo** and to achieve high drug loading. As shown in Fig. S4a (supporting information), **Ir1lipo** and **Ir2lipo** were transparent and show light yellow and orange with an encapsulation efficiency of 95.4% and 97.2%, respectively. As can be seen from Fig. S4b (supporting information), the average particle size of blank liposome, **Ir1lipo** and **Ir2lipo** were 102.0 ± 3.6, 158.4 ± 2.02, 131.6 ± 1.94 nm with PDI of 0.307, 0.054, 0.122, respectively. These results indicated that the liposomes are homogeneous and stable because of the low PDI (Polydispersity index) value. In addition, the Zeta potential of blank liposome, **Ir1lipo** and **Ir2lipo** are −16.46 ± 2.44, −17.40 ± 0.92 and − 16.03 ± 2.64 mV, respectively (Fig. S4c, supporting information), which further indicates that the liposomes were relatively stable (10–20 mV) [45].

3.2. In vitro drug release studies of liposomes

The release of **Ir1** and **Ir2** from **Ir1lipo** and **Ir2lipo** was carried out in PBS (pH = 7.4) containing 0.5% Tween 80 (*w/v*), at 37 °C and rotated at 200 rpm by dialysis methods. As shown in Fig. S5 (supporting information), the percentage of cumulative drug release of **Ir1lipo** and **Ir2lipo** at 4 h reached 13.63 ± 0.81% and 16.34 ± 0.52%, respectively. At 84 h, the cumulative rates of **Ir1lipo** and **Ir2lipo** reached the highest values of 37.53% and 38.72%. During the process of release, the cumulative release rate increased gradually, and the cumulative release rate of **Ir2lipo** was always higher than that of **Ir1lipo**. The in vitro release profile of the liposomes showed that **Ir1** and **Ir2** from liposomes **Ir1lipo** and **Ir2lipo** was slowly performed.

3.3. pK_a values determination

To determine the value of the acid dissociation constant (pK_a), the complexes were titrated in water-acetonitrile mixtures (*v*/v, 7:3) over a pH range of 2 to 10. Acidic drugs ($pK_a < 4$) or basic drugs ($pK_a > 10$) can't cross the cell membrane by passive diffusion [46]. The pH values of the complexes **Ir1** and **Ir2** in water-acetonitrile mixtures are 6.47 and 6.64. The titration curves for **Ir1** and **Ir2** were shown in Fig. S6 (Supporting Information), the pK_a values are 6.60 and 6.79 for **Ir1** and **Ir2**, respectively, indicating that the complexes can cross the cell membrane and enter the cell. The complexes exhibit weak acidity due to the dissociation of the N—H proton in the imidazole ring [47].

Table 1
IC_{50} (μM) values of DBIPB, **Ir1**, **Ir2**, **Ir1lipo** and **Ir2lipo** toward selected cancer cells for 48 h.

Complex	SGC-7901	HepG2	A549	HeLa	B16	NIH3T3
DBIPB	48.2 ± 3.5	> 200	> 200	36.6 ± 3.8	78.4 ± 5.1	> 200
Ir1	> 200	> 200	> 200	> 200	> 200	> 200
Ir1lipo	4.7 ± 0.2	16.0 ± 1.4	14.5 ± 0.4	6.3 ± 0.2	7.9 ± 0.9	23.4 ± 0.7
Ir2	> 200	> 200	> 200	> 200	> 200	> 200
Ir2lipo	12.4 ± 0.5	24.1 ± 1.0	22.0 ± 0.2	12.5 ± 0.4	14.4 ± 0.8	24.5 ± 1.2

3.4. Cytotoxicity in vitro assays

The cytotoxicity of DBIPB, **Ir1**, **Ir2**, **Ir1lipo** and **Ir2lipo** toward SGC-7901, HepG2, A549, HeLa, B16 tumor cells and normal NIH3T3 cells was determined using 3-(4,5-dimethylthiazole-2-yl)-2,5-biphenyl tetrazolium bromide (MTT) assays. As observed from Table 1, ligand DBIPB, **Ir1** and **Ir2** showed no inhibitory effect on the cell proliferation against the selected cell lines in vitro. Although the pK_a values indicated that the complexes may cross cell membranes, low solubility of **Ir1** and **Ir2** in PBS inducing the less amounts of complexes entering the cells resulted in no cytotoxic activity. To enhance anticancer activity, the complexes were encapsulated in the liposomes by ethanol injection, it is easy for the complexes-loaded liposomes to enter the cells, thereby increasing the cellular uptake. As expected, the liposomes **Ir1lipo** and **Ir2lipo** displayed noticeable toxicity, especially for SGC-7901 cells with a low IC_{50} value of 4.7 ± 0.2 and 12.4 ± 0.5 μM. The cytotoxic activity of **Ir1lipo** and **Ir2lipo** is comparable to iridium(III) complex ([Ir(ppy)$_2$(TFPIP)] (PF_6))-loaded liposome (IC_{50} = 7.6 ± 0.5 μM, TFPIP = 2-(4′-trifluoromethyl)-[1,1′-biphenyl]-4-yl)-1*H*-imidazo[4,5-f][1,10]phenanthroline) [24]. Additionally, we also evaluated the cytotoxicity in vitro of blank liposomes and we found that the blank liposomes have no cytotoxic activity against the selected cancer and normal cells. Similar results can be discovered in our previous work [38], hence, the blank liposomes show no interference on the activity of **Ir1lipo** and **Ir2lipo**. In addition, the cytotoxicity of **Ir1**, **Ir2**, **Ir1lipo** and **Ir2lipo** follows the trend of **Ir1lipo** > **Ir2lipo** > **Ir1** ≈ **Ir2**. Hence, for the complexes with low solubility, liposomes are an effective carrier to deliver drug and increase the anticancer efficacy.

3.5. Uptake of complexes and liposomes

Liposomes are a new structure for encapsulating and delivering bioactive agents, which are characterized by high permeability to hydrophobic drugs and low permeability to hydrophilic drugs, carrying the active molecules to specific sites of action and releasing them slowly [48,49]. To verify that liposomes encapsulated complexes can enter tumor cells through the cell membrane, SGC-7901 cells were treated with IC_{50} concentration of **Ir1**, **Ir2**, **Ir1lipo** and **Ir2lipo** for 24 h and the cells were stained with DAPI. As seen in Fig. 1a, the cell nuclei were stained blue with DAPI, the complexes or their liposomes emit bright green fluorescence, moreover, the green fluorescence emitted by the liposomes is stronger than those emitted by **Ir1** and **Ir2**. The overlap of green and blue showed that the complexes and their liposomes can be successfully uptaken by the cells. The uptaken amounts of **Ir1lipo** and

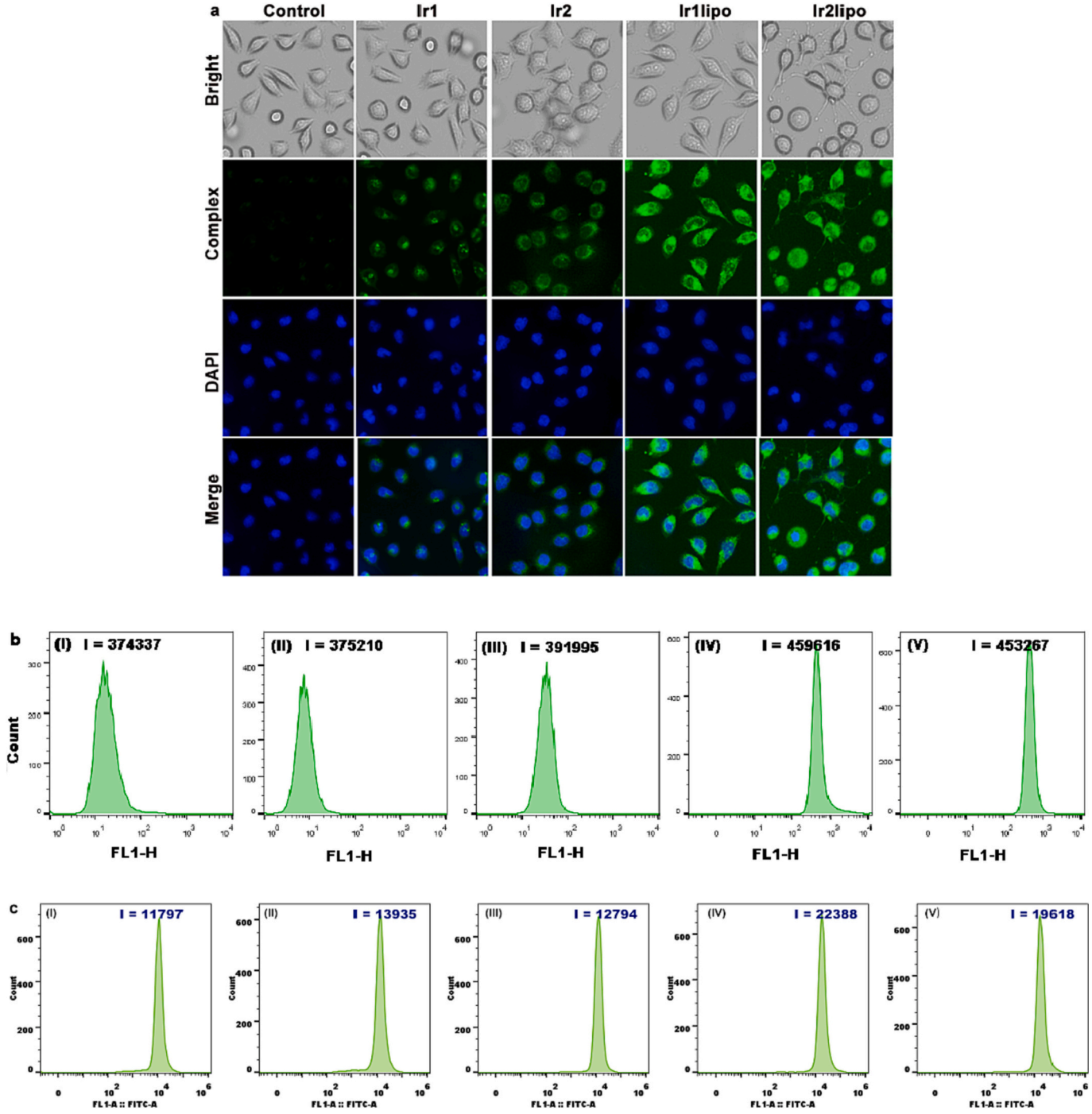

Fig. 1. (a) Cellular uptake was assayed after an exposure of SGC-7901 cells to IC_{50} concentration of **Ir1**, **Ir2**, **Ir1lipo** and **Ir2lipo** for 24 h and the cells were stained with DAPI. The cellular uptake was investigated using flow cytometry after treatment of SGC-7901 cells (b, I) and NIH3T3 cells (c, I) with IC_{50} concentration **Ir1** (II), **Ir2** (III), **Ir1lipo** (IV) and **Ir2lipo** (V) for 24 h.

Ir2lipo are larger than those of **Ir1** and **Ir2**.

The cellular uptake of complexes and their liposomes was further investigated using flow cytometry. As illustrated in Fig. 1b, the fluorescence intensity value in the control (I) was 374,337, the green fluorescence intensity only increased by 0.23% and 4.72% in the **Ir1** and **Ir2**-treated groups. However, the fluorescence intensity increased by 22.78% and 21.08% in the **Ir1lipo** and **Ir2lipo**-treated groups compared with that in the control after 24 h of exposure of SGC-7901 cells to **Ir1lipo** (IV) and **Ir2lipo** (V). We also determined the cell uptake of **Ir1**, **Ir1lipo**, **Ir2** and **Ir2lipo** by normal NIH3T3 cells, as shown in Fig. 1c, NIH3T3 cells (I) were exposed to IC_{50} concentration **Ir1** (II), **Ir2** (III), **Ir1lipo** (IV) and **Ir2lipo** (V) for 24 h, the green fluorescence intensity increased by 18.12% for **Ir1**, 8.45% for **Ir2**, 89.78% for **Ir1lipo** and 66.29% for **Ir2lipo**, respectively, which is consistent with cytotoxicity of complexes and complex-loaded liposomes toward NIH3T3 cells. The results confirmed that the complexes encapsulated into liposomes have high cell membrane permeability.

3.6. Inhibiting cell growth with 3D model

Cancer cells grown in two-dimensional (2D) monolayer culture usually lose their tissue specificity, while multicellular tumor spheroids

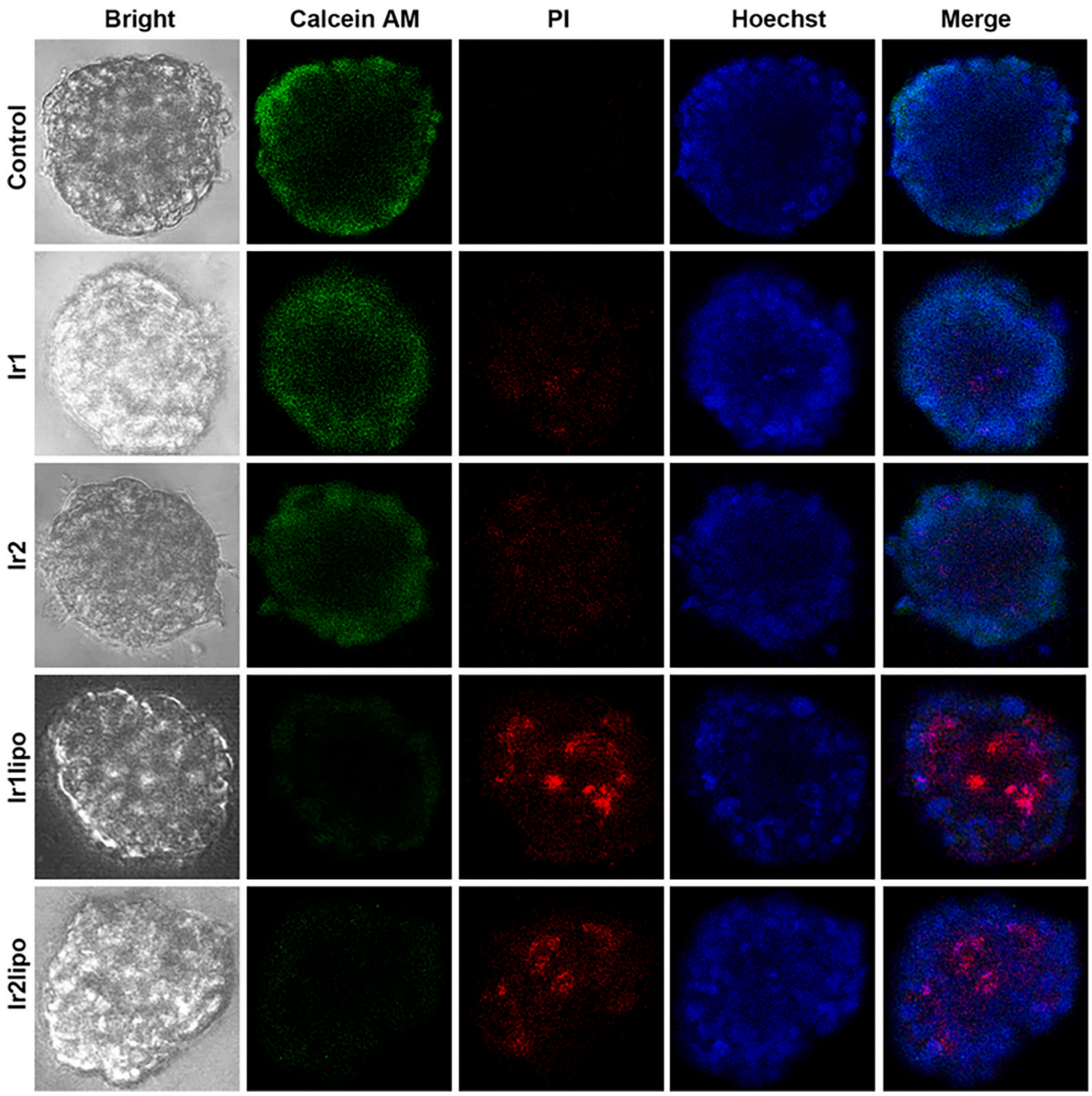

Fig. 2. Confocal microscopy images of the 3D SGC-7901 MCTSs after treatment with IC_{50} concentration of **Ir1**, **Ir2**, **Ir1lipo** and **Ir2lipo** for 24 h and the live/dead cells were stained with Calcein AM/PI.

(MCTSs) referred to as 3D in vitro models can reproduce the sophisticated microenvironment of solid tumors in vivo [50]. MCTSs reflect the natural cellular behaviors and metabolic properties of cancer differentiation, invasion and metastasis bridging the limitations of screening the pathophysiology of anticancer drugs in 2D cell cultures [51,52]. To further determine the ability of **Ir1**, **Ir2**, **Ir1lipo** and **Ir2lipo** to prevent cell growth, Calcein AM (Calcein Acetoxymethyl Ester) and PI (propidium iodide) were used to stain living and dead cells, respectively. As shown in Fig. 2, the cells in the control spheroids and **Ir1** and **Ir2**-treated groups grew well with the bright green fluorescence (calcein AM, live cells). In contrast, in the IC_{50} concentration of **Ir1lipo** and **Ir2lipo** groups, the 3D model showed very low green fluorescence and the significantly enhanced red fluorescence (PI, dead cells), which demonstrated that most of the cells were dead in SGC-7901 MCTSs. The results further demonstrated that **Ir1lipo** and **Ir2lipo** display higher anticancer activity than **Ir1** and **Ir2** under the same conditions.

3.7. Cell invasion studies

Malignant tumor cells can infiltrate the lymphatic system and blood vessels and metastasize to distant organs, resulting in metastatic spread and treatment failure [53]. In vitro scratch assay is a simple, versatile and effective method to study collective cell migration and wound healing [54]. Therefore, the scratch assay was used to assess the inhibitory effect of the **Ir1**, **Ir2**, **Ir1lipo** and **Ir2lipo** on the migratory capacity of SGC-7901 cells. As shown in Fig. S7a (supporting information), **Ir1** and **Ir2** attenuated the healing of cellular wounds to a certain extent compared to the control, but still did not prevent the tendency of tumor cells to migrate. However, the cells were treated with IC_{50} concentration of **Ir1lipo** and **Ir2lipo** for 24 h, the width of the wound was almost unchanged, and the cell migration was effectively inhibited. Focal adhesion kinase (FAK) is a non-receptor tyrosine kinase with a key role in regulating cell migration, spreading and adhesion and survival of cells [55]. In cancer, FAK is a major driver of invasion and metastasis [56]. Western blot analysis showed that **Ir1lipo** and **Ir2lipo** significantly

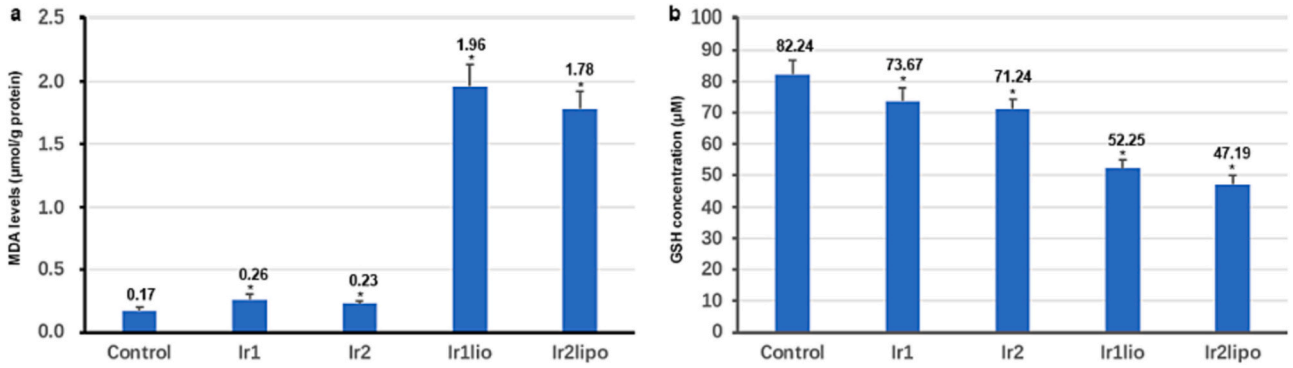

Fig. 3. The determination of intracellular MDA (a) and GSH (b) in SGC-7901 treated with IC_{50} concentration of **Ir1**, **Ir2**, **Ir1lipo** and **Ir2lipo** for 24 h. The difference was significant when $^{*}P < 0.05$.

inhibited FAK protein expression after an incubation of SGC-7901 cells with IC_{50} concentration of **Ir1lipo** and **Ir2lipo** for 24 h compared with the control (Fig. S7b, supporting information). In summary, **Ir1lipo** and **Ir2lipo** can inhibit the migration, spreading and adhesion of SGC-7901 cells through a downregulation of FAK protein.

3.8. *Effect of the liposomes on autophagy*

Autophagy is a conserved cellular degradation process whereby cellular organelles and proteins are engulfed by autophagosomes, digested within lysosomes, and recycled to maintain cellular homeostasis [57,58]. Dysregulation of autophagy can lead to the development of various diseases, including tumor development, and higher levels of autophagy induce cell death [59]. Autophagy occurs with the upregulation of Beclin-1 expression and the conversion of LC3-I into LC3-II, which is a hallmark of autophagy [60]. The extent of autophagy occurrence induced by **Ir1**, **Ir2**, **Ir1lipo** and **Ir2lipo** were evaluated using the specific dye monodansylcadaverine (MDC). As shown in Fig. S8a (supporting information), In the control or **Ir1** and **Ir2**-treated groups, weak green fluorescence was found, indicating no occurrence of

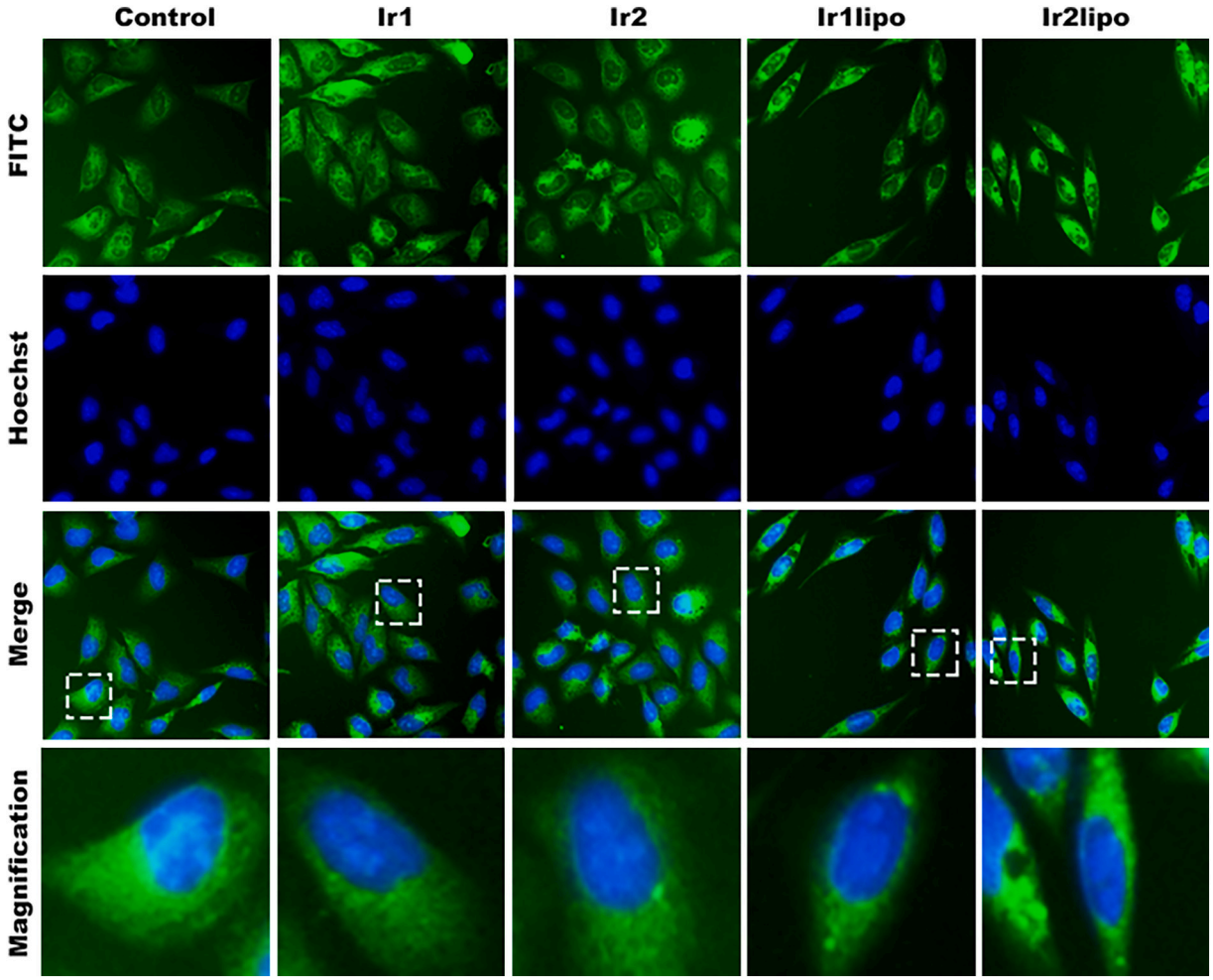

Fig. 4. Assays of microtubules network of SGC-7901 induced by IC_{50} concentration of **Ir1**, **Ir2**, **Ir1lipo** and **Ir2lipo** for 24 h.

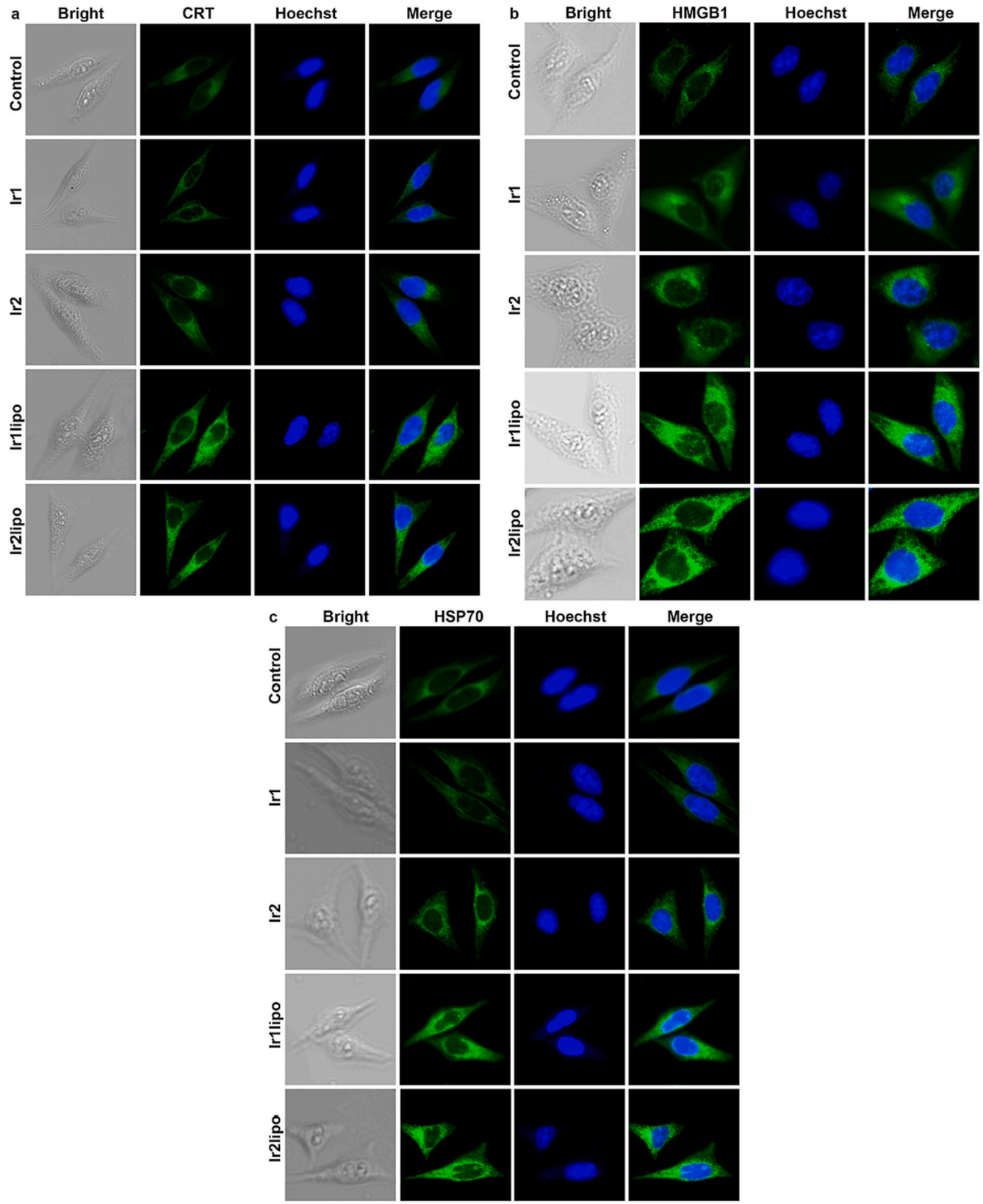

Fig. 5. Images of CRT (a), HMGB1 (b) and HSP70 (c) levels after SGC-7901 cells incubated with IC_{50} concentration of **Ir1**, **Ir2**, **Ir1lipo** and **Ir2lipo** for 24 h.

autophagy. However, bright green fluorescence was observed after SGC-7901 cells were exposed to IC_{50} concentration of **Ir1lipo** and **Ir2lipo** for 24 h. The results showed that **Ir1lipo** and **Ir2lipo** significantly induced autophagy. The expression of Beclin-1 and LC3 proteins was assayed by western blot, as presented in Fig. S8bc (supporting information), **Ir1lipo** and **Ir2lipo** significantly increased the expression of Beclin-1 and prompted the conversion of LC3-I into LC3-II. These results further confirmed that **Ir1lipo** and **Ir2lipo** can effectively induce autophagy in

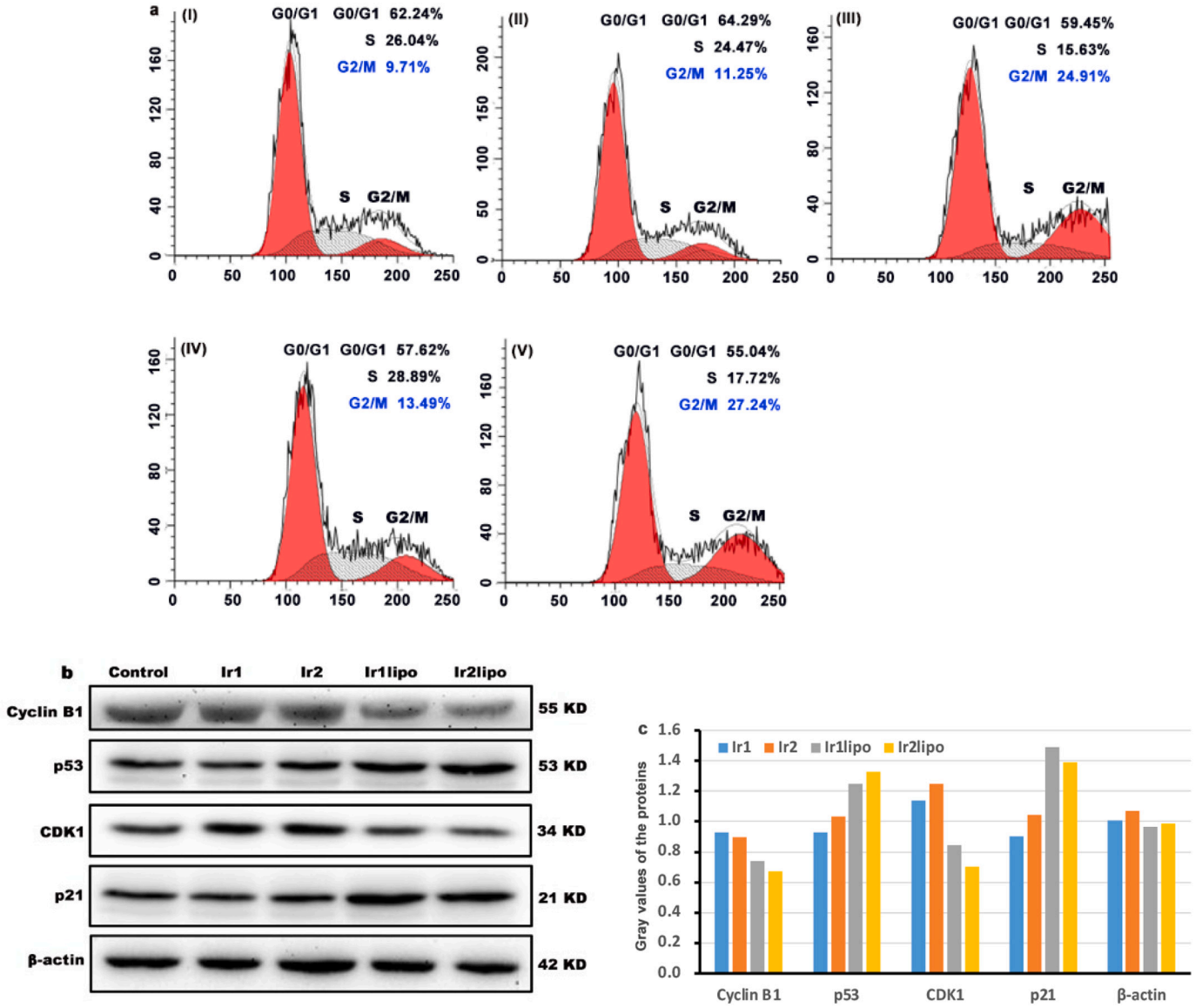

Fig. 6. (a) Cell cycle distribution of SGC-7901 cells (I) treated with IC_{50} concentration of **Ir1** (II), **Ir2** (IV), **Ir1lipo** (III) and **Ir2lipo** (V) for 24 h. (b) The expression of Cyclin B1, p53, CDK1 and p21 proteins after SGC-7901 cells were treated with IC_{50} concentration of **Ir1**, **Ir2**, **Ir1lipo** and **Ir2lipo** for 24 h. (c) The quantitative values of the expression of Cyclin B1, p53, CDK1, p21 and β-actin was used as the internal control.

SGC-7901 cells.

3.9. The location of the liposomes at the endoplasmic reticulum

The endoplasmic reticulum (ER) is the central organelle for the biosynthesis, folding, assembly and trafficking of secreted proteins and transmembrane proteins, which determines the survival function of cells [61,62]. To determine the target organelle of the complexes and liposomes, SGC-7901 cells were incubated with IC_{50} concentration of **Ir1**, **Ir2**, **Ir1lipo** and **Ir2lipo** for 4 h at 37 °C and observed under the ImageXpress Micro XLS System. As can be seen from Fig. S9 (supporting information), the endoplasmic reticulum was stained bright red with ER-Tracker Red, the cellular nuclei were stained blue with Hoechst, furthermore, the green fluorescence associated with **Ir1lipo** and **Ir2lipo** was stronger than those of **Ir1** and **Ir2**. The overlap of red and green fluorescence indicated that the complexes and their liposomes locate at endoplasmic reticulum. The Pearson's colocalization coefficients (PCC) were obtained by analyzing the red and green fluorescence intensity in 50 cells with the software image pro plus (version 6.0). The PCC values are 0.97 for **Ir1**, 0.98 for **Ir2**, 0.98 for **Ir1lipo** and 0.99 for **Ir2lipo**, indicating an existence of positive correlation. The results reveal that the complexes and their liposomes target the endoplasmic reticulum.

3.10. Intracellular MDA and GSH detection

Oxidative stress is the factor that often contributes to cytotoxicity and apoptosis [63]. To determine the impact of **Ir1**, **Ir2**, **Ir1lipo** and **Ir2lipo** on oxidative damage, the amount of peroxidation product malondialdehyde (MDA) was measured to estimate the lipid peroxidation extent of SGC-7901 cells. As displayed in Fig. 3a, MDA concentrations were elevated significantly after the treatment of SGC-7901 cells with IC_{50} concentration of **Ir1lipo** and **Ir2lipo** for 24 h, whereas the complexes **Ir1** and **Ir2** showed a slight effect on the lipid peroxidation. Glutathione (GSH) is an intracellular antioxidant that plays an important role in maintaining redox homeostasis by protecting cells from oxidative damage and detrimental xenobiotics [64]. As depicted in Fig. 3b, intracellular GSH content was significantly reduced after 24 h of treatment of SGC-7901 with IC_{50} concentration of the complexes and

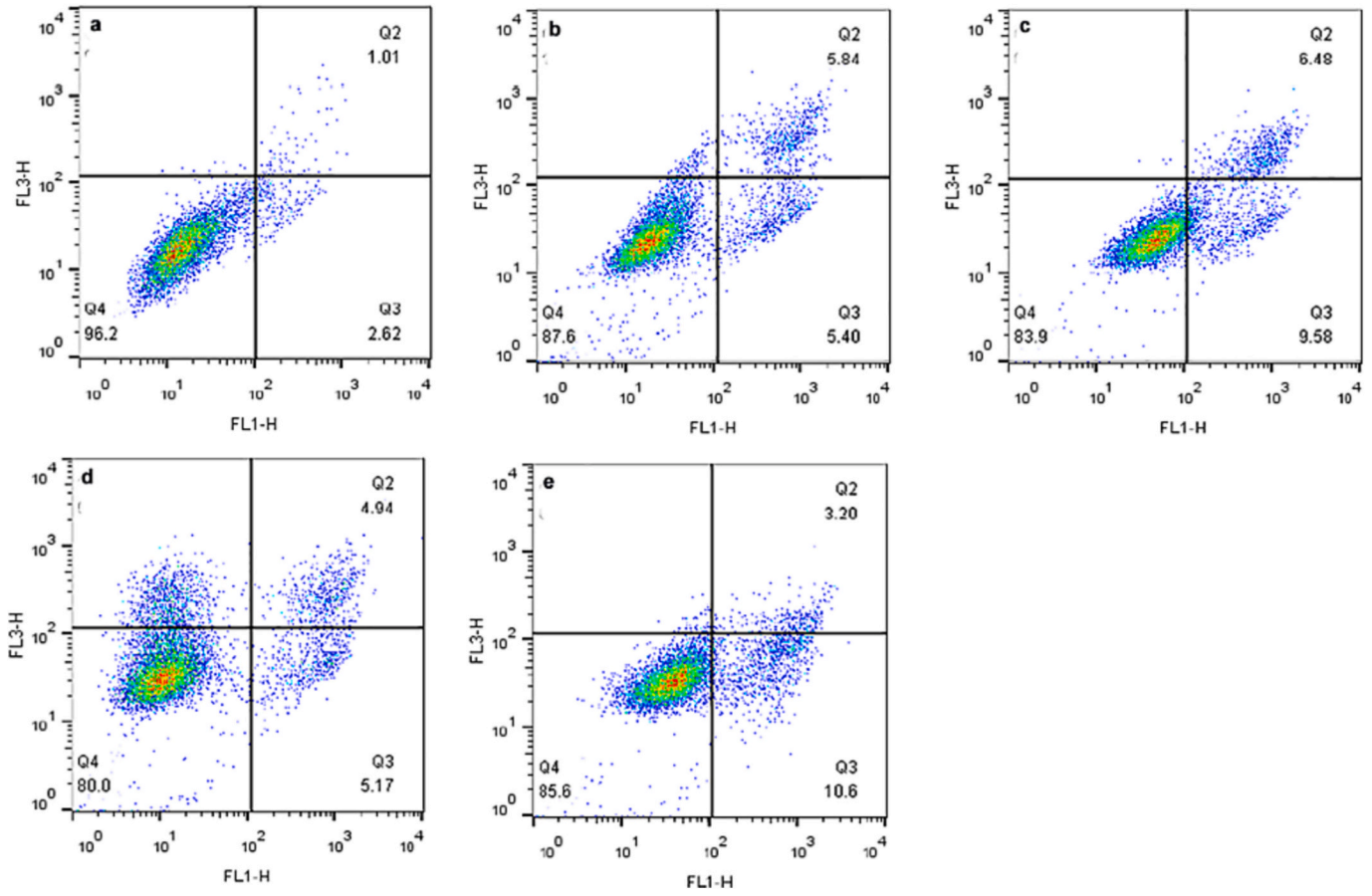

Fig. 7. The apoptosis percentage of SGC-7901 cells (a) treated with IC_{50} concentration of **Ir1** (b), **Ir1lipo** (c), **Ir2** (d) and **Ir2lipo** (e) for 24 h. Q2, Q3 and Q4 stand forlate, early apoptosis and living cells.

liposomes compared to the control, while the ratios of GSH/GSSG (glutathione disulfide) in the control, **Ir1**, **Ir2**, **Ir1lipo** and **Ir2lipo**-treated groups are 6.05 ± 1.58, 5.78 ± 1.73, 5.28 ± 1.13, 4.53 ± 1.41 and 5.11 ± 1.36, respectively. The inhibition of GSH production in cells and reduction of cellular antioxidant capacity follow the order of **Ir2lipo** > **Ir1lipo** > **Ir2** > **Ir1**. The results suggested that **Ir1lipo** and **Ir2lipo** can effectively inhibit GSH biosynthesis and promote lipid peroxidation causing oxidative damage to SGC-7901 cells.

3.11. Effect of the complexes and their liposomes on microtubule networks

Microtubules are cytoskeletal filaments composed of α and β tubulin subunits that play an important role in chromosome division and translocation as well as cell motility in cancer cells [65]. In addition, tubulin is an established target of various successful anticancer drugs and disruption of microtubules is a major mechanism for inhibiting the growth of rapidly dividing cells [66]. As shown in Fig. 4, in the control, SGC-7901 cells were complete in morphology, showing irregular polygonal shape, full of cytoplasm, and microtubules were dispersed radially to the surrounding. After **Ir1** (4.7 μM) and **Ir2** (12.4 μM) incubation, the cell morphology was almost indistinguishable from that of the control and showed no effect on microtubule polymerization. However, the morphology of IC_{50} concentration of **Ir1lipo** and **Ir2lipo**-treated cells was significantly altered, with tumor cells being shuttle-shaped, cytoplasm contracting and microtubules becoming blurred. The results confirmed that **Ir1lipo** and **Ir2lipo** can exert antitumor effects through inhibiting tubulin polymerization.

3.12. Immunogenic cell death (ICD) assays

Immunogenic cell death (ICD) is a unique cell death featured by the activation of dying cell immune response and release of damage associated molecular patterns (DAMPs) [67,68]. ICD is characterized by the high expression level of the calreticulin (CRT), heat shock protein 70 (HSP70), high mobility group box 1 (HMGB1) [69]. To further evaluate the ICD effects induced by the ER-targeted complexes and liposomes, SGC-7901 cells were incubated with IC_{50} concentration of **Ir1**, **Ir2**, **Ir1lipo** and **Ir2lipo** for 24 h and CRT, HSP70, HMGB1 were explored. As shown in Fig. 5, SGC-7901 cells elicited by **Ir1lipo** and **Ir2lipo** treatment, translocation of CRT (a) to the cell membrane from ER, release of HMGB1 (b) and high expression of HSP70 (c) from the nuclei to the extracellular environment were identified. Overall, the results suggest that **Ir1lipo** and **Ir2lipo** localized at the ER, causing oxidative stress damage which effectively induced immunogenic cell death.

3.13. Cell cycle arrest analysis

Cancer is thought to be a result of cell cycle dysregulation and inhibition of cell proliferation is thought to be a common mechanism for anti-cancer drugs [70]. To investigate the arresting effect of the cycle of the complexes and liposomes, flow cytometry was used to determine the cell cycle phase distribution. As illustrated in Fig. 6a, SGC-7901 cells (I) were treated with IC_{50} concentration of **Ir1** (II), **Ir1lipo** (III), **Ir2** (IV) and **Ir2lipo** for 24 h, compared to the control, a slight increase of 1.54% for **Ir1**, 3.78% for **Ir2** in the percentage of SGC-7901 cells at the G2/M phase was discovered. However, the liposomes **Ir1lipo** and **Ir2lipo** induced an increase of 15.20% and 17.53% in the percentage of the cells at the G2/M phase, respectively. Hence, **Ir1lipo** and **Ir2lipo** showed

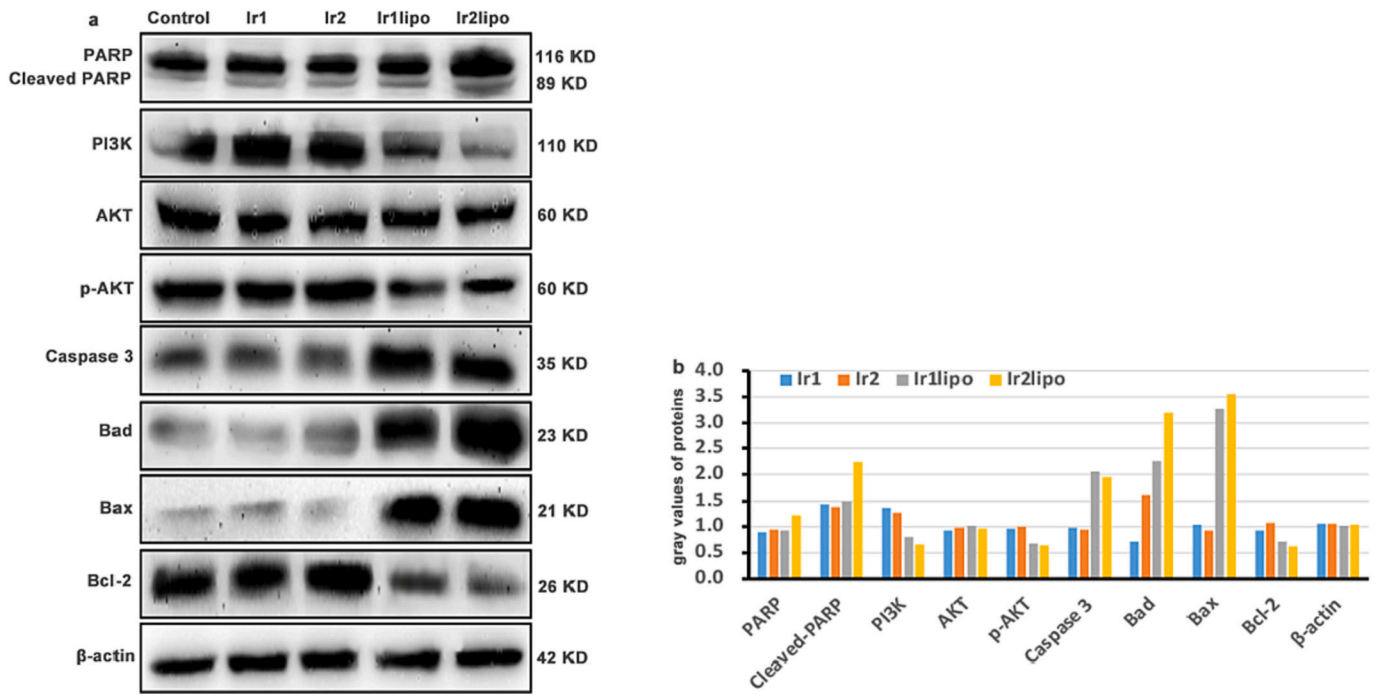

Fig. 8. (a) The expression levels of PARP, Cleaved-PARP, PI3K, AKT, p-AKT, Caspase 3, Bad, Bax and Bcl-2 in SGC-7901 cells after treatment of SGC-7901 cells with IC_{50} concentration of **Ir1**, **Ir2**, **Ir1lipo** and **Ir2lipo** for 24 h. (b) Densitometric quantification of the expression of PARP, Cleaved-PARP, PI3K, AKT, p-AKT, Caspase 3, Bad, Bax and Bcl-2 and β-actin was used an internal control.

higher inhibitory efficacy on the cell cycle arrest than complexes **Ir1** and **Ir2** under the same conditions. The results demonstrated that liposomes **Ir1lipo** and **Ir2lipo** significantly inhibited cell proliferation at the G2/M phase.

When cells damage occurs, the tumor suppressor p53 is activated and causes high levels of p21 (the cyclin-dependent kinase inhibitor) expression, triggering the downregulation of related cell cycle genes and inhibiting cell cycle arrest [71]. Cyclin B1 interacts with the cyclin-dependent kinase 1 (CDK1) to form an active heterodimer that guides the G2 phase cells into the M phase [72,73]. To further confirm the cell cycle arrest, the expression of related proteins was investigated using western blot. As can be seen from Fig. 6b, the expression of p21 and p53 proteins increased after incubation with IC_{50} concentration of **Ir1lipo** and **Ir2lipo**. Conversely, the expression of Cyclin B1 and CDK1 proteins that promote cell division and proliferation were inhibited, while **Ir1** and **Ir2** show no obvious effect on the expression of Cyclin B1, p53, CDK1, p21. The quantitative values of the expression of Cyclin B1, p53, CDK1, p21 and β-actin are shown in Fig. 6c. The results clearly show that **Ir1lipo** and **Ir2lipo** induce cell cycle arrest at the G2/M phase through activating the p21/p53 signal pathway and inhibition of Cyclin B1/CDK1 heterodimer formation in the SGC-7901 cells.

3.14. Apoptosis studies

Apoptosis is widely known as programmed cell death and plays an important role in cancer [74]. To explore the apoptotic function of **Ir1**, **Ir2**, **Ir1lipo** and **Ir2lipo**, the SGC-7901 cells were stained with FITC (fluorescein isothiocyanate)-labeled Annexin V (3′,6′-dihydroxy-5-isothiocyanato-3H-spiro(isobenzofuran-1,9′-xanthen)-3-one) and PI (propidium iodide) and quantified using flow cytometry. As revealed in Fig. 7, in the control (a), the percentage of early apoptosis is 2.62%. After an exposure of 24 h of SGC-7901 cells to IC_{50} concentration of **Ir1** (b), **Ir2** (d), **Ir1lipo** (c) and **Ir2lipo** (e), an increase of 2.78% for **Ir1**, 6.96% for **Ir1lipo**, 2.55% for **Ir2**, 7.88% for **Ir2lipo**, respectively. **Ir1lipo** and **Ir2lipo** show higher apoptotic effect than **Ir1** and **Ir2** under the identical conditions.

3.15. Release of cytochrome c and PI3K/AKT signaling pathway

B-cell lymphoma-2 (Bcl-2) family proteins locate in the mitochondria through altering mitochondrial membrane permeability and promoting leakage of the apoptotic factor cytochrome *c*, which activates caspases induces intrinsic apoptosis [75,76]. Caspases are a family of conserved cysteine proteases that play key roles in apoptosis, poly(ADP-ribose) polymerase (PARP) as a cleavage substrate for Caspase 3, and expression of Cleaved-PARP is thought to be a marker for the onset of apoptosis [77,78]. The release of cytochrome *c* was detected by immunofluorescence staining. As indicated in Fig. S10 (supporting information), compared to the control, exposure of SGC-7901 cells to IC_{50} concentration of **Ir1** and **Ir2** for 24 h resulted in a slight effect on the release of cytochrome *c*. However, the fluorescence intensity after a 24 h treatment of SGC-7901 cells with IC_{50} concentration of **Ir1lipo** and **Ir2lipo** was significantly increased, indicating that cytochrome *c* was efficiently released into the cytoplasm. In addition, the protein levels of Bcl-2 family proteins were determined by western blot. As revealed in Fig. 8a, **Ir1lipo** and **Ir2lipo** significantly upregulated the expression of Bad (Bcl-2-associated death) and Bax (Bcl-2-associated X) proteins and downregulated the expression of anti-apoptosis proteins Bcl-2 (B-cell lymphoma-2). The expression of Caspase 3 and Cleaved-PARP, which were downstream regulatory signals of apoptosis, were significantly increased.

To further explore the effects of **Ir1**, **Ir2**, **Ir1lipo** and **Ir2lipo** on apoptosis initiation and its possible mechanisms of action, western blotting was utilized to detect PI3K (phosphatidylinositol 3-kinase)-AKT (protein kinase B) pathway. The results showed that after treatment of SGC-7901 cells with IC_{50} concentration of **Ir1lipo** and **Ir2lipo** for 24 h, the expression of PI3K was inhibited, the expression of phosphorylated AKT (p-AKT) was significantly reduced, while the expression of AKT levels was not obviously changed (Fig. 8a and **b**), **Ir1** and **Ir2** show weak effect on the Bcl-2 family proteins. Overall, these results demonstrated that **Ir1lipo** and **Ir2lipo** induced apoptosis in SGC-7901 via regulating Bcl-2 family proteins and inhibiting the PI3K/AKT signaling pathway.

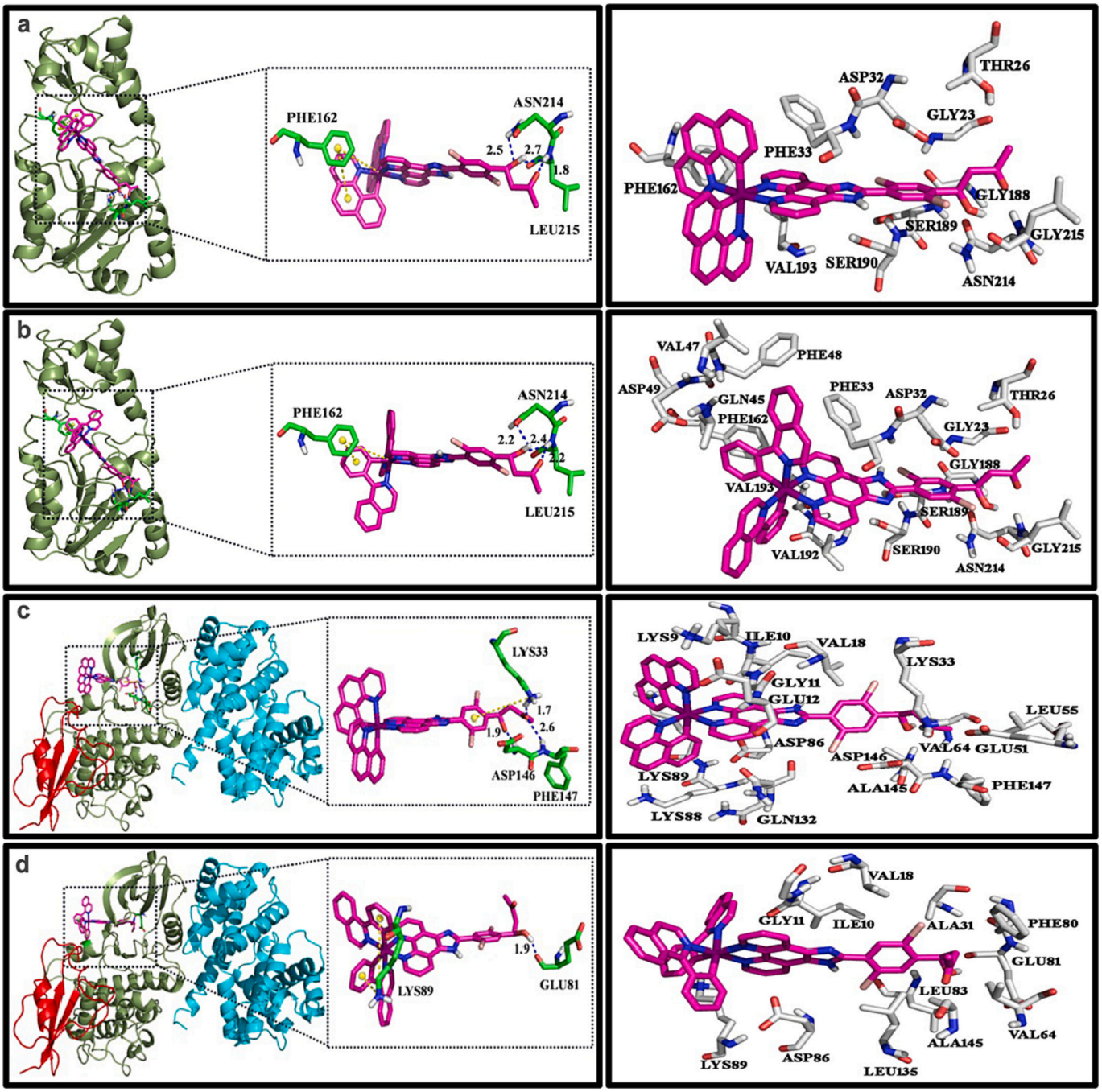

Fig. 9. The binding of the complexes with p53 (PDB: 4BUZ)(**Ir1** a and **Ir2** b), CDK1 (PDB: 5LQF) (**Ir1** c and **Ir2** d).

Table 2
The lowest binding energies of the complexes with proteins.

Complexes	p53	CDK1	p21	PARP	PI3K	Caspase 3	Bad	Bax	Bcl-2
Ir1	−12.50	−11.05	−9.16	−11.68	−9.04	−9.04	−9.08	−6.73	−7.68
Ir2	−13.07	−10.26	−10.03	−11.79	−8.37	−8.37	−9.43	−7.05	−9.05

3.16. Molecular docking studies

To assess the affinity of liposome loading **Ir1** and **Ir2** with the target proteins, we performed a molecular docking analysis using Autodock Vina (version 1.2.2). The method validation was performed using crystallized and docking ligand. Binding poses, interactions and the binding energies generated by each interaction of the complexes with p53, CDK1, p21, PARP, PI3K, caspase 3, Bad, Bax and Bcl-2 were obtained. As shown in Fig. 9, the complexes **Ir1** and **Ir2** interact with p53, CDK1 through hydrogen bond (The binding of the complexes with p21 (PDB: 5E0U), PARP (PDB: 4PJV), PI3K (PDB: 1e8x), caspase 3 (PDB: 1GFW), Bad (PDB: 1G5J), Bax (PDB: 2K7W), Bcl-2 (PDB: 4LVT) is shown in Fig. S11, supporting information). The lowest binding energies are listed in Table 2. Complexes **Ir1** and **Ir2** show large binding affinities

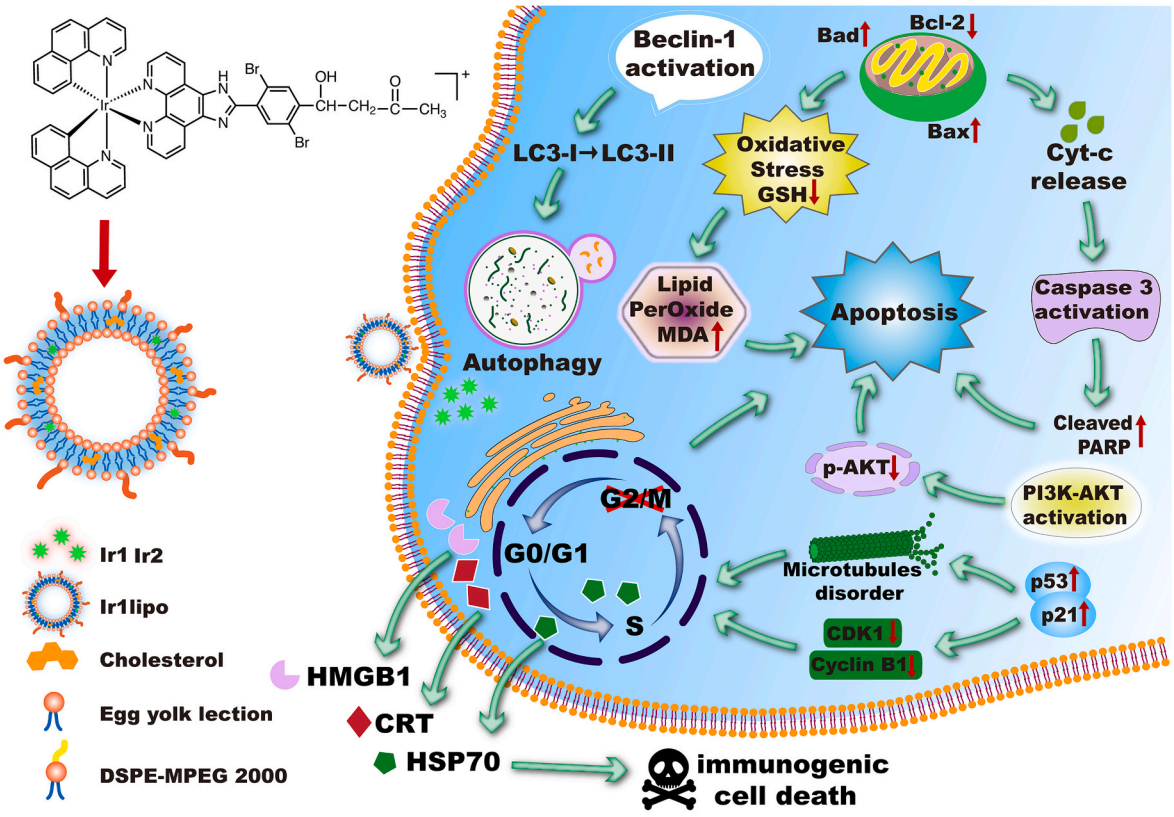

Fig. 10. The molecular mechanism of **Ir1lipo** and **Ir2lipo** inducing apoptosis in SGC-7901 cells.

with p53, CDK1, p21 and PARP proteins.

4. Conclusions

In this study, two iridium(III) complexes $[Ir(bzq)_2(DIPH)](PF_6)$ (**Ir1**) and $[Ir(piq)_2(DIPH)](PF_6)$ (**Ir2**) were synthesized and characterized. **Ir1** and **Ir2** have no cytotoxicity toward SGC-7901, HepG2, HeLa, A549, B16 and normal NIH3T3 cells. When the complexes were encapsulated into the liposomes **Ir1lipo** and **Ir2lipo**, **Ir1lipo** and **Ir2lipo** exhibit high cytotoxic activity against SGC-7901 cells. Compared to **Ir1** and **Ir2**, the liposome **Ir1lipo** and **Ir2lipo** significantly increased the uptake of SGC-7901 cells and inhibited the invasion and metastasis of tumor cells. On the other hand, **Ir1lipo** and **Ir2lipo** inhibit tubulin polymerization and regulated the expression cycle of p53 and p21 proteins arresting the cell cycle at the G2/M phase. The studies on apoptotic mechanism indicated that **Ir1lipo** and **Ir2lipo** induced apoptosis through inhibiting the PI3K/AKT signaling pathway and triggering Bcl-2 family activation further promoting the release of cytochrome *c* and activation of Caspase 3 to cleave PARP. In addition, **Ir1lipo** and **Ir2lipo** colocalize at the endoplasmic reticulum, generate ER-stress to induce immunogenic cell death (ICD), inhibit GSH biosynthesis, promote lipid peroxidation to impair antioxidant capacity (Fig. 10). This work demonstrates that complexes-loaded liposomes greatly enhance the anticancer activity of iridium(III) complexes and provides a help for the design and synthesis of new effective iridium(III) complexes as potent anticancer reagents.

Author statement

We state that the manuscript has been finished by all authors listed in the manuscript. The all data are original and real. We agree to be accountable for all aspects of the work to ensure that questions related to the accuracy or integrity of any part of the work are appropriately investigated and resolved.

All authors have read the manuscript and approved the manuscript to be submitted to JIB.

Declaration of Competing Interest

Authors declare no competing interests exist.

Data availability

Data will be made available on request.

Acknowledgments

This work was supported by the National Natural Science Foundation of China (No 21877018).

Appendix A. Supplementary data

Supplementary data to this article can be found online at https://doi.org/10.1016/j.jinorgbio.2023.112134.

References

[1] R.L. Siegel, K.D. Miller, H.E. Fuchs, A. Jemal, Cancer statistics, CA Cancer J. Clin. Densitom. 72 (2022) (2022) 7–33.
[2] H. Sung, J. Ferlay, R.L. Siegel, M. Laversanne, I. Soerjomataram, A. Jemal, F. Bray, Global Cancer Statistics, GLOBOCAN estimates of incidence and mortality worldwide for 36 cancers in 185 countries, CA Cancer J. Clin. 71 (2021) (2020) 209–249.
[3] A.P. Thrift, H.B. El-Serag, Burden of gastric cancer, Clin. Gastroenterol. Hepatol. 18 (2020) 534–542.
[4] K.X. Li, A. Zhang, X.Y. Li, H.T. Zhang, L.M. Zhao, Advances in clinical immunotherapy for gastric cancer, Biochim. Biophys. Acta Rev. Cancer. 1876 (2021), 188615.
[5] A. Patel, Benign vs malignant tumors, JAMA Oncol. 6 (2020) 1488.
[6] J. Massagué, A.C. Obenauf, Metastatic colonization by circulating tumor cells, Nature. 529 (2016) 298–306.

[7] M. Brock, A. Kanapathipillai, D.E. Ingber, Nanoparticle targeting of anti-cancer drugs that alter intracellular signaling or influence the tumor microenvironment, Adv. Drug Deliv. Rev. 79-80 (2014) 107–118.

[8] J.P. Gao, W. Xu, W.T. Liu, M. Yan, Z.G. Zhu, Tumor heterogeneity of gastric cancer: from the perspective of tumor-initiating cell, World J. Gastroenterol. 24 (2018) 2567–2581.

[9] C. D'Alterio, S. Scala, G. Sozzi, L. Roz, G. Bertolini, Paradoxical effects of chemotherapy on tumor relapse and metastasis promotion, Semin. Cancer Biol. 60 (2020) 351–361.

[10] N. Joharatnam-Hogan, K.K. Shiu, K. Khan, Challenges in the treatment of gastric cancer in the older patient, Cancer Treat. Rev. 85 (2020), 101980.

[11] G.Q. Wei, Y. Wang, G. Yang, Y. Wang, R. Ju, Recent progress in nanomedicine for enhanced cancer chemotherapy, Theranostics. 11 (2021) 6370–6392.

[12] M. Davern, J. Lysaght, Cooperation between chemotherapy and immunotherapy in gastroesophageal cancers, Cancer Lett. 495 (2020) 89–99.

[13] B. Rosenberg, L. VanCamp, J.E. Trosko, V.H. Mansour, Platinum compounds: a new class of potent antitumor agents, Nature. 222 (1969) 385–386.

[14] F.P. Harmers, W.H. Gispen, J.P. Neijt, Neurotoxic side-effects of cisplatin, Eur. J. Cancer 27 (1991) 372–376.

[15] A. Calls, A. Torres-Espin, X. Navarro, V.J. Yuste, E. Udina, J. Bruna, Cisplatin-induced peripheral neuropathy is associated with neuronal senescence-like response, Neuro-Oncology 23 (2021) 88–99.

[16] R. Oun, Y.E. Moussa, N.J. Wheate, The side effects of platinum-based chemotherapy drugs: a review for chemists, Dalton Trans. 47 (2018) 6645–6653.

[17] S. Rottenberg, C. Disler, P. Perego, The rediscovery of platinum-based cancer therapy, Nat. Rev. Cancer 21 (2021) 37–50.

[18] L. Biancalana, H. Kostrhunova, L.K. Batchelor, M. Hadiji, I. Degano, G. Pampaloni, S. Zacchini, P.J. Dyson, V. Brabec, F. Marchetti, Hetero-bis-conjugation of bioactive molecules to half-sandwich ruthenium(II) and iridium(III) complexes provides synergic effects in cancer cell cytotoxicity, Inorg. Chem. 60 (2021) 9529–9541.

[19] L.L. Wang, R.L. Guan, L.N. Xie, X.X. Liao, K. Xiong, T.W. Rees, Y. Chen, L.N. Ji, H. Chao, An ER-targeting iridium(III) complex that induces immunogenic cell death in non-small-cell lung cancer, Angew. Chem. Int. Ed. Eng. 60 (2021) 4657–4665.

[20] J.W. Wang, H.M. Liu, X.Y. Wu, C.L. Shi, W.L. Li, Y.H. Yuan, Y.J. Liu, D.G. Xing, Induction of apoptosis in SGC-7901 cells by iridium(III) complexes via endoplasmic reticulum stress-mitochondrial dysfunction pathway, J. Biol. Inorg. Chem. 27 (2022) 455–469.

[21] J. Hao, H.M. Liu, J.W. Wang, X.Z. Wang, C.X. Huang, L.J. Liang, J. Chen, Y. Wang, Y.J. Liu, Iridium(III) complexes induce cervical carcinoma apoptosis via disturbing cellular redox homeostasis disorder and inhibiting PI3K/AKT/mTOR pathway, J. Inorg. Biochem. 235 (2022), 111946.

[22] J.C. Shen, T.W. Rees, L.N. Ji, H. Chao, Recent advances in ruthenium(II) and iridium(III) complexes containing nanosystems for cancer treatment and bioimaging, Coord. Chem. Rev. 443 (2021), 214016.

[23] W.J. Wang, Y.Y. Ling, Y.M, Zhong, Z.Y. Li, C.P. Tan, Z.W. Mao, Ferroptosis-enhanced cancer immunity by a ferrocene-appended iridium(III) diphosphine complex, Angew. Chem. Int. Ed. Eng. 61 (2022) e202115247.

[24] H.W. Zhang, X.F. Liao, X.Y. Wu, C.L. Shi, Y.Y. Zhang, Y.H. Yuan, W.L. Li, J. W. Wang, Y.J. Liu, Iridium(III) complexes entrapped in liposomes trigger mitochondria-mediated apoptosis and GSDME-mediated pyroptosis, J. Inorg. Biochem. 228 (2022), 111706.

[25] Y.H. Yuan, C.L. Shi, X.Y. Wu, W.L. Li, C.X. Huang, L.J. Liang, J. Chen, Y. Wang, Y. J. Liu, Synthesis and anticancer activity in vitro and in vivo evaluation of iridium (III) complex on mouse melanoma B16 cells, J. Inorg. Biochem. 232 (2022), 111820.

[26] G. Gupta, S. Cherukommu, G. Srinivas, S.W. Lee, S.H. Mun, BODIPY-based Ru(II) and Ir(III) organometallic complexes of avobenzone, a sunscreen material: potent anticancer agents, J. Inorg. Biochem. 189 (2018) 17–29.

[27] G. Gupta, P. Kumair, J.Y. Ryu, J. Lee, S.M. Mobin, C.Y. Lee, Mitochondrial localization of highly fluorescent and photostable BODIPY-based ruthenium(II), rhodium(III), and iridium(III) metal complexes, Inorg. Chem. 58 (2018) 8587–8595.

[28] Z. Liu, P.J. Sadler, Organoiridium complexes: anticancer agents and catalysts, Acc. Chem. Res. 47 (2014) 1174–1185.

[29] Y.H. Yuan, Y.Y. Zhang, J. Chen, C.X. Huang, H.M. Liu, W.L. Li, L.J. Liang, Y. Wang, Y.J. Liu, Synthesis, biological evaluation of novel iridium(III) complexes targeting mitochondria toward melanoma B16 cells, Eur. J. Med. Chem. 247 (2023), 115046.

[30] J. Zhao, Y. Gao, W.Y. He, W. Wang, W.W. Hu, Y.Y. Sun, Synthesis, characterization and biological evaluation of two cyclometalated iridium(III) complexes containing a glutathione S-transferase inhibitor, J. Inorg. Biochem. 238 (2023), 112050.

[31] Z. Cheng, M.Y. Li, R. Dey, Y.H. Chen, Nanomaterials for cancer therapy: current progress and perspectives, J. Hematol. Oncol. 14 (2021) 85.

[32] T. Minamisakamoto, S. Nishiguchi, K. Hashimoto, K.I. Ogawara, M. Maruyama, K. Higaki, Sequential administration of PEG-span 80 niosome enhances anti-tumor effect of doxorubicin-containing PEG liposome, Eur. J. Pharm. Biopharm. 169 (2021) 20–28.

[33] S.V. Morse, A. Mishra, T.G. Chan, R.T.M. de Rosales, J.J. Choi, Liposome delivery to the brain with rapid short-pulses of focused ultrasound and microbubbles, J. Control. Release 341 (2022) 605–615.

[34] P.E. Saw, J. Park, E. Lee, S. Ahn, J. Lee, H. Kim, J. Kim, M. Choi, F.O.C. Arokhzad, S. Jon, Effect of PEG pairing on the efficiency of cancer-targeting liposomes, Theranostics. 5 (2015) 746–754.

[35] D.X. Liu, J. Cohen, N. Turkman, PEG2000-DBCO surface coating increases intracellular uptake of liposomes by breast cancer xenografts, Sci. Rep. 12 (2022) 10564.

[36] P.P. Goli, M.B. Torbati, K. Parivar, A.A. Khiavi, M. Yousefi, Preparation and evaluation of gemcitabin and cisplatin-entrapped folate-PEGylated liposomes as targeting co-drug delivery system in cancer therapy, J. Drug Deliv. Sci. Technol. 65 (2021), 102756.

[37] Y.Y. Zhang, W.D. Fei, H.W. Zhang, Y. Zhou, L. Tian, J. Hao, Y.H. Yuan, W.L. Li, Y. J. Liu, Increasing anticancer effect in vitro and vivo of liposome-encapsulated iridium(III) complexes on BEL-7402 cells, J. Inorg. Biochem. 225 (2021), 111622.

[38] L. Bai, W.D. Fei, Y.Y. Gu, M. He, F. Du, W.Y. Zhang, L.L. Yang, Y.J. Liu, Liposomes encapsulated iridium(III) polypyridyl complexes enhance anticancer activity in vitro and in vivo, J. Inorg. Biochem. 205 (2020), 111014.

[39] Y.Y. Gu, L. Bai, Y.Y. Zhang, H.W. Zhang, D.G. Xing, L. Tian, Y. Zhou, J. Hao, Y. J. Liu, Liposome as drug delivery system enhance anticancer activity of iridium(III) complex, J. Lipo. Res. 31 (2021) 342–355.

[40] W.L. Li, X.Y. Wu, H.M. Liu, C.L. Shi, Y.H. Yuan, L. Bai, X.F. Liao, Y.Y. Zhang, Y. J. Liu, Enhanced in vitro cytotoxicity and antitumor activity in vivo of iridium(III) complexes liposomes targeting endoplasmic reticulum and mitochondria, J. Inorg. Biochem. 233 (2022), 111868.

[41] M. Yamada, Y. Tanaka, Y. Yoshimoto, S. Kuroda, I. Shimao, Synthesis and properties of diamino-substituted dipyrido [3,2-a:2′,3′-c]phenazine, Bull. Chem. Soc. Jpn. 65 (1998) 1006–1011.

[42] S. Sprouse, K.A. King, P.J. Spellane, R.J. Watts, Photophysical effects of metal-carbon σ bonds in ortho-metallated complexes of Ir(III) and Rh(III), J. Am. Chem. Soc. 106 (1984) 6647–6653.

[43] C. Jaafar-Maalej, R. Diab, V. Andrieu, A. Elaissari, H. Fessi, Ethanol injection method for hydrophilic and lipophilic drug-loaded liposome preparation, J. Lipo. Res. 20 (2010) 228–243.

[44] T. Mosmann, Rapid colorimetric assay for cellular growth and survival: application to proliferation and cytotoxicity assays, J. Immunol. Methods 65 (1983) 55–63.

[45] H. Kouchakzadeh, S.A. Shojaosadati, A. Maghsoudi, E.V. Farahani, Optimization of PEGylation conditions for BSA nanoparticles using response surface methodology, AAPS Pharm. Sci. Tech. 11 (2010) 1206–1211.

[46] D.T. Manallack, The pK(a) distribution of drugs: application to drug discovery, Perspect. Med. Chem. 1 (2007) 25–38.

[47] P. Pal, T. Ganguly, S. Das, S. Baitalik, pH-responsive colorimetric, emission and redox switches based on Ru(ii)-terpyridine complexes, Dalton Trans. 50 (2021) 186–196.

[48] G. Bozzuto, A. Molinari, Liposomes as nanomedical devices, Int. J. Nanomedicine 10 (2015), 975–799.

[49] Y. Panahi, M. Farshbaf, M. Mohammadhosseini, M. Mirahadi, R. Khalilov, S. Saghfi, A. Akbarzadeh, Recent advances on liposomal nanoparticles: synthesis, characterization and biomedical applications, Artif. Cells Nanomed. Biotechnol. 4 (2017) 788–799.

[50] C.R. Thoma, M. Zimmermann, I. Agarkova, J.M. Kelm, W. Krek, 3D cell culture systems modeling tumor growth determinants in cancer target discovery, Adv. Drug Deliv. Rev. 69-70 (2014) 29–41.

[51] L.P. Ferreira, V.M. Gaspar, J.F. Mano, Design of spherically structured 3D in vitro tumor models -advances and prospects, Acta Biomater. 75 (2018) 11–34.

[52] S. Li, K.F. Yang, X.Y. Chen, X.L. Zhu, H.Y. Zhou, P. Li, Y. Chen, Y. Jiang, T.T. Li, X. Qin, H. Yang, C.H. Wu, B. Ji, F.M. You, Y.Y. Liu, Simultaneous 2D and 3D cell culture array for multicellular geometry, drug discovery and tumor microenvironment reconstruction, Biofabrication. 13 (2021) 4.

[53] Q. Ma, L.C. Dieterich, K. Ikenberg, S.B. Bachmann, J. Mangana, S.T. Proulx, V. C. Amann, M.P. Levesque, R. Dummer, P. Baluk, D.M. McDonald, M. Detmar, Unexpected contribution of lymphatic vessels to promotion of distant metastatic tumor spread, Sci. Adv. 4 (2018) eaat4758.

[54] A. Grada, M. Otero-Vinas, F. Prieto-Castrillo, Z. Obagi, V. Falanga, Research techniques made simple: analysis of collective cell migration using the wound healing assay, J. Invest. Dermatol. 137 (2017) e11–e16.

[55] P. Tapial Martínez, P. López Navajas, D. Lietha, FAK structure and regulation by membrane interactions and force in focal adhesions, Biomolecules. 10 (2020) 179.

[56] A. Spallarossa, B. Tasso, E. Russo, C. Villa, C. Brullo, The development of FAK inhibitors: a five-year update, Int. J. Mol. Sci. 23 (2022) 6381.

[57] T. Yamazaki, J.M. Bravo-San Pedro, L. Galluzzi, G. Kroemer, F. Pietrocola, Autophagy in the cancer-immunity dialogue, Adv. Drug Deliv. Rev. 169 (2021) 40–50.

[58] M. Ishaq, R. Ojha, A.P. Sharma, S.K. Singh, Autophagy in cancer: recent advances and future directions, Semin. Cancer Biol. 66 (2020) 171–181.

[59] M.C. Maiuri, E. Zalckvar, A. Kimchi, G. Kroemer, Self-eating and self-killing: crosstalk between autophagy and apoptosis, Nat. Rev. Mol. Cell Biol. 8 (2007) 741–752.

[60] X.H. Li, S.K. He, B.Y. Ma, Autophagy and autophagy-related proteins in cancer, Mol. Cancer 19 (2020) 12.

[61] X. Chen, J.R. Cubillos-Ruiz, Endoplasmic reticulum stress signals in the tumour and its microenvironment, Nat. Rev. Cancer 21 (2021) 71–88.

[62] H.W. Moon, H.G. Han, Y.J. Jeon, Protein quality control in the endoplasmic reticulum and cancer, Int. J. Mol. Sci. 19 (2018) 3020.

[63] K. Środa-Pomianek, K. Michalak, P. Świątek, A. Poła, A. Palko-Łabuz, O. Wesołowska, Increased lipid peroxidation, apoptosis and selective cytotoxicity in colon cancer cell line LoVo and its doxorubicin-resistant subline LoVo/Dx in the presence of newly synthesized phenothiazine derivatives, Biomed. Pharmacother. 106 (2018) 624–636.

[64] B.Y. Niu, K.X. Liao, Y.X. Zhou, T. Wen, G.L. Quan, X. Pan, C.B. Wu, Application of glutathione depletion in cancer therapy: enhanced ROS-based therapy, ferroptosis, and chemotherapy, Biomaterials. 277 (2021), 121110.
[65] A.E. Prota, K. Bargsten, J.F. Diaz, M. Marsh, C. Cuevas, M. Liniger, C. Neuhaus, J. M. Andreu, K.H. Altmann, M.O. Steinmetz, A new tubulin-binding site and pharmacophore for microtubule-destabilizing anticancer drugs, Proc. Natl. Acad. Sci. U. S. A. 111 (2014) 13817–13821.
[66] D.K. Sigalapalli, V. Pooladanda, P. Singh, M. Kadagathur, S.D. Guggilapu, J. L. Uppu, N.D. Tangellamudi, P.K. Gangireddy, C. Godugu, N.B. Bathini, Discovery of certain benzyl/phenethyl thiazolidinone-indole hybrids as potential anti-proliferative agents: synthesis, molecular modeling and tubulin polymerization inhibition study, Bioorg. Chem. 92 (2019), 103188.
[67] M.Z. Jin, X.P. Wang, Immunogenic cell death-based cancer vaccines, Front. Immunol. 12 (2021), 697964.
[68] D.V. Krysko, A.D. Garg, A. Kaczmarek, O. Krysko, P. Agostinis, P. Vandenabeele, Immunogenic cell death and DAMPs in cancer therapy, Nat. Rev. Cancer 12 (2012) 860–875.
[69] A. Ahmed, S.W.G. Tait, Targeting immunogenic cell death in cancer, Mol. Oncol. 14 (2020) 2994–3006.
[70] J.J. Nair, J. van Staden, Cell cycle modulatory effects of amaryllidaceae alkaloids, Life Sci. 213 (2018) 94–101.
[71] K. Engeland, Cell cycle regulation: p53-p21-RB signaling, Cell Death Differ. 29 (2022) 946–960.
[72] S. Lim, P. Kaldis, Cdks, cyclins and CKIs: roles beyond cell cycle regulation, Development. 140 (2013) 3079–3093.
[73] M. Castedo, J.L. Perfettini, T. Roumier, G. Kroemer, Cyclin-dependent kinase-1: linking apoptosis to cell cycle and mitotic catastrophe, Cell Death Differ. 9 (2002) 1287–1293.
[74] O. Morana, W. Wood, C.D. Gregory, The apoptosis paradox in cancer, Int. J. Mol. Sci. 23 (2022) 1328.
[75] X.J. Jiang, X.D. Wang, Cytochrome C-mediated apoptosis, Annu. Rev. Biochem. 73 (2004) 87–106.
[76] N. Zamzami, G. Kroemer, The mitochondrion in apoptosis: how pandora's box opens, Nat. Rev. Mol. Cell Biol. 2 (2001) 67–71.
[77] A. Bressenot, S. Marchal, L. Bezdetnaya, J. Garrier, F. Guillemin, F. Plénat, Assessment of apoptosis by immunohistochemistry to active caspase-3, active caspase-7, or cleaved PARP in monolayer cells and spheroid and subcutaneous xenografts of human carcinoma, J. Histochem. Cytochem. 57 (2009) 289–300.
[78] F.J. Oliver, G. de la Rubia, V. Rolli, M.C. Ruiz-Ruiz, G. de Murcia, J.M. Murcia, Importance of poly (ADP-ribose) polymerase and its cleavage in apoptosis. Lesson from an uncleavable mutant, J. Biol. Chem. 27 (1998) 33533–33539.